International Journal of Heat and Mass Transfer 121 (2018) 170–186

Contents lists available at ScienceDirect

International Journal of Heat and Mass Transfer

journal homepage: www.elsevier.com/locate/ijhmt

Numerical study on condensation heat transfer and pressure drop characteristics of ethane/propane mixture upward flow in a spiral pipe

Shulei Li [a,b], Weihua Cai [a,*], Jie Chen [c], Haochun Zhang [a], Yiqiang Jiang [b,*]

[a] School of Energy Science and Engineering, Harbin Institute of Technology, Harbin, China
[b] Building Thermal Energy Engineering, Harbin Institute of Technology, Harbin, China
[c] CNOOC Gas and Power Group, Beijing, China

ARTICLE INFO

Article history:
Received 18 September 2017
Received in revised form 3 December 2017
Accepted 28 December 2017
Available online 5 January 2018

Keywords:
Hydrocarbon mixture
Condensation heat transfer
Pressure drop
Spiral pipe
Numerical simulation

ABSTRACT

Spiral wound heat exchanges (SWHE) has been the most widely used in large-scale liquid natural gas (LNG) plants. However, few studies have been focused on the condensation heat transfer and pressure drop for hydrocarbon mixture refrigerant in SWHE tube side. In this paper, the condensation heat transfer and pressure drop characteristics for ethane/propane mixture upward flow in a spiral pipe were numerically investigated. The numerical model was established and verified based on the existing experimental results and new flow pattern observation experiments. It discussed the variation trends of void fraction, frictional pressure drop, heat transfer coefficient and heat and mass transfer resistance with various parameters, such as, vapor quality, mass flux, heat flux, saturation pressure and inclination angle. Comparing with the existing correlations, the results showed that Steiner's correlation, modified Fuchs's correlation, Boyko's correlation could better predict the void fraction, frictional pressure drop, film heat transfer coefficient with mean absolute deviation of 6.08%, 10.67% and 13.06%, respectively. Meanwhile, modified Silver approach was used to modify the mixed effects of ethane/propane mixture on heat transfer. The study provides some constructive instructions to understand the condensation of zeotropic mixtures in the spiral pipe, and is helpful in designing more effective SWHE.

1. Introduction

Spiral wound heat exchanger (SWHE) (as shown in Fig. 1) is probable the most comment type of main cryogenic exchanger in large-scale liquid natural gas (LNG) plants since its multi-stream capability, high compactness, efficient heat transfer, sufficient flexibility and better robustness [1–4]. Meanwhile, hydrocarbon mixtures are usually used as working medium in LNG field. Therefore, the condensation flow and heat transfer for hydrocarbon mixtures is the main phenomenon in SWHE tube side. However, due to its complex, such as the mixed effect of zeotropic mixtures, it is still insufficient to understand this phenomenon in a spiral tube. A better understanding of this phenomenon can be contributed to the design and optimization of SWHE. The geometric parameters of common LNG SWHE are shown in Table 1.

Until now, there are many studies on condensation of zeotropic mixtures in tubes. Fronk and Garimella [7] reviewed experimental and analytical results corresponding on the coupled heat and mass transfer phenomena during condensation of different zeotropic fluid mixtures in tubes. In this paper, it showed that for zeotropic mixtures, the heat and mass transfer resistances in vapor and liquid phases increased the overall heat transfer resistance beyond what would be expected from a weighted average of corresponding resistances for pure components. From an experimental viewpoint, Berrada et al. [8] measured condensation heat transfer coefficients for R23/R134a refrigerant mixtures at three different component ratios in a horizontal tube to appreciate the glide effect on heat transfer. The results showed that no glide effect on heat transfer coefficients was observed. However, Shao et al. [9] found that a greater temperature glide would lead a greater degradation of heat transfer coefficients for R32/R134a mixtures, especially at low mass flux. Shao et al. [10,11] also experimentally investigated the condensation flow and heat transfer of pure, azeotropic and zeotropic refrigerants in a horizontal tube. The results indicated that for pure, azeotropic and zeotropic refrigerants with a small temperature glide, heat transfer coefficients were independent on mass flux in wavy flow regions, and increased with the increasing mass flux in annular flow regions; but for other zeotropic refrigerants, it always increased with the increase of mass flux within tested ranges. Eckels et al. [12] compared the average condensation heat transfer coefficients of R32/R134a mixtures with those of R22 in a

* Corresponding authors.
E-mail addresses: caiwh@hit.edu.cn (W. Cai), jyq7245@sina.com (Y. Jiang).

https://doi.org/10.1016/j.ijheatmasstransfer.2017.12.140
0017-9310/

Nomenclature

A_{lv} interfacial area density between liquid phase and vapor phase, m^{-1}
ARD average deviation, Eq. (50)
Bo Boiling number, $Bo=q/(m\gamma_{lv})$
C_D drag coefficient, $C_D = 0.44$
C_μ, $C_{\varepsilon 1}$, $C_{\varepsilon 2}$ constant with the values of 0.09, 1.44 and 1.92, respectively
C_f Correction factor of the two-phase enhancement at the interface on vapor core heat transfer
Cp specific heat at constant pressure, J/(kg K)
d hydraulic diameter, m
d_{lv} mean interfacial length scale between the liquid phase and vapor phase, m
D curvature diameter, m
f friction factor
$\vec{f}_{\sigma,lv}$ surface force acting on vapor phase due to the presence of the liquid phase per unit area, N/m^2
$\vec{F}_{lv}$ interfacial forces acting on liquid phase due to the presence of the vapor phase, N/m^3
$\vec{F}_{D,lv}$ drag force acting on vapor phase due to the presence of the liquid phase per unit volume, N/m^3
$\vec{F}_{\sigma,lv}$ surface force acting on vapor phase due to the presence of the liquid phase per unit volume, N/m^3
Fr_{l0} full-liquid Froude number, $Fr_{l0} = m^2/(\rho_l^2 gd)$
Fr_{tp} mixture Froude number, $Fr_{tp} = m^2/(gd\rho_{tp}^2)$
g gravity acceleration, m/s^2
h heat transfer coefficient, $W/(m^2 K)$
h_{film}, h_{core}, h_{mix} the liquid film, vapor core and mixed heat transfer coefficient, respectively, $W/(m^2{\cdot}K)$
h'_v the smooth gas superficial single-phase heat transfer coefficient
h_v, h_l heat transfer coefficient of liquid phase and vapor phase on one side of the phase interface, respectively, $W/(m^2 K)$
h_{lv} heat transfer coefficient between vapor phase side and liquid phase side, $W/(m^2 K)$
k turbulent kinetic energy, m^2/s^2
L length of test section, m
m mass flux, $kg/(m^2 s)$
$\dot{m}_{lv}$ mass flow rate in per unit interfacial area from vapor phase to liquid phase, $kg/(m^2 s)$
MARD mean absolute deviation, Eq. (51)
$\vec{n}_{lv}$ interface normal vector pointing from liquid phase to the vapor phase
Nu_{lv} Nusselt number between vapor phase side and liquid phase side, $Nu_{lv} = h_{lv}d_{lv}/\lambda_{lv}$
p pressure, Pa
P saturation pressure, Pa
P_{cr} critical pressure, Pa
P_k turbulence production, Pa/s
P_{kbi} buoyancy turbulence production, Pa/s
Pr Prandtl number, $Pr = \mu Cp/\lambda$
q heat flux, W/m^2
q_{tot}, q_{core} the total, vapor core heat flux, respectively, W/m^2
q_v, q_l sensible interphase heat transfer to the vapor phase across the interface with the liquid phase and to the liquid phase across the interface with the vapor phase per unit volume, respectively, W/m^3
Q_v, Q_l total interphase heat transfer to the vapor phase across the interface with the liquid phase and to the liquid phase across the interface with the vapor phase per unit volume, respectively, W/m^3
Re_{eq} equivalent Reynolds number, $Re_{eq} = m[1 - x + x(\rho_l/\rho_v)^{0.5}]d/\mu_l$
Re_l liquid Reynolds number, $Re_l = m(1-x)d/\mu_l$
Re_{l0} full-liquid Reynolds number, $Re_{l0} = md/\mu_l$
Re_v vapor Reynolds number, $Re_v = mdx/\mu v$
T temperature, K
T_c vapor core temperature, K
u velocity, m/s
We_{tp} mixture Weber number, $We_{tp} = m^2 d/(\sigma\rho_{tp}^2)$
x vapor quality
X_{tt} Lockhart-Martinelli parameter, $X_{tt} = [(1-x)/x]^{0.9}(\rho_v/\rho_l)^{0.5}(\mu_l/\mu_v)^{0.1}$
Z the ratio between sensible to total heat flux

Greek symbols

α volume fraction or void fraction
β inclination angle
ρ density, kg/m^3
μ dynamic viscosity, Pa s
μ_t turbulent viscosity, Pa s
λ thermal conductivity, W/(m K)
γ enthalpy, J/kg
γ_{lv} latent heat of phase change, J/kg
γ_{vS}, γ_{lS} interfacial values of enthalpy carried into vapor phase and liquid phase due to phase change, respectively, J/kg
σ surface tension coefficient, N/m
σ_k, σ_ε constant with the values of 1.3 and 1.0, respectively
δ the liquid film thickness, m
δ_{lv} interface delta function, m^{-1}
ΔP_f Frictional pressure drop, Pa/m
κ_{lv} surface curvature, m^{-1}
θ Correction factor of mass transfer on vapor core heat transfer
ε turbulent dissipation rate, m^2/s^3
ξ condensation heat ratio
φ_{lv} two-phase enhancement factor, $\varphi_{lv} = \left[\left(\frac{dp}{dl}\right)_{tp} - \left(\frac{dp}{dl}\right)_{l0}\right] \Big/ \left[\left(\frac{dp}{dl}\right)_{v0} - \left(\frac{dp}{dl}\right)_{l0}\right]$
ϕ_{l0}^2 full-liquid frictional pressure drop multiplier, $\phi_{l0}^2 = \left(\frac{dp}{dl}\right)_{tp} \Big/ \left(\frac{dp}{dl}\right)_{l0}$
ϕ_v^2 vapor frictional pressure drop multiplier
Φ heat and mass transfer resistance in vapor core for mixtures, $K\,m^2\,W^{-1}$, $\Phi = Z/h_{core}$
ψ_{l0} ratio of the two-phase and full-liquid single phase heat transfer coefficient, $\psi_{l0} = h_{film,s}/h_{l0}$
Γ_{lv} mass flow rate in per unit volume from vapor phase to liquid phase, $kg/(m^3 s)$
Γ_{lv}^+ positive mass flow rate in per unit volume from vapor phase, $kg/(m^3 s)$

Subscripts

c, s coiled or straight pipe
cr critical
exp experimental value
i any
l liquid phase
$l0$ all the mass flux is taken as liquid
pre predicted value
ref reference
sat saturation
sim simulated value
S interfacial
t turbulent
tp two phase
v vapor phase
$v0$ all the mass flux is taken as vapor

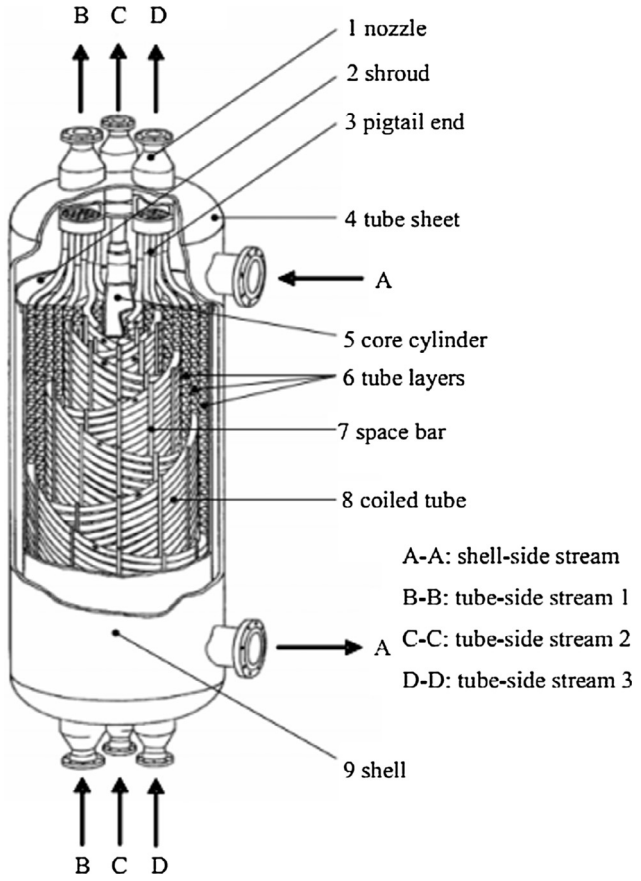

Fig. 1. A schematic of a multi-stream SWHE [5].

horizontal pipe and found that the R32 (45%)/R125 (55%) mixture had slightly better heat transfer performance than R22, while the R32 (25%)/R125 (75%) mixture had significantly lower heat transfer performance than R22. Smit et al. [13] measured condensation heat transfer coefficients of R22/R142b mixture at different mass fractions in a horizontal tube and found that at low mass flux, condensation heat transfer coefficients decreased with the increasing fraction of R142b, but at high mass flux, they were not strongly influenced by the refrigerant mass fraction. A series of experimental studies on condensation heat transfer and pressure drop characteristics of R410A–oil mixture in horizontal smooth and microfin tubes were carried out by Huang et al. [14–17]. The results stated that whether in smooth or microfin tubes, the presence of oil always deteriorated heat transfer. However, in smooth tubes, the presence of oil always decreased frictional pressure drop at all vapor qualities while in microfin tubes, the presence of oil decreased frictional pressure drop at lower vapor qualities, but increased it at higher vapor qualities. Thonon et al. [18] researched the condensation heat transfer for pure and mixtures of hydrocarbons in a compact plate heat exchanger. It is found that with the increase of Reynolds numbers, for pure fluids, heat transfer coefficients decreased at laminar regime, but increased at turbulent regime; however, for mixtures, heat transfer coefficients always increased. Macdonald et al. [19] also investigated the condensation of hydrocarbon mixtures inside horizontal tubes at different diameters. The results revealed that the decrease of heat transfer coefficient due to mixture effects was the most significant at large temperature glides and in a larger tube diameter, but was the least significant at higher mass fluxes. Neeraas [20] proposed an experimental study on the heat transfer and pressure drop characteristics of hydrocarbon mixtures condensation inside a coil-wound tube and found that Fuchs's correlation [21] corrected by density ratios at high pressure and vapor quality was suitable to calculate

Table 1
Geometric parameters of LNG SWHE [6].

Height	Curvature diameter	Inclination angle	Length of single tube	Tube diameter
10–50 m	1–3 m	5–15°	70–100 m	10–15 mm

Table 2
Summary of experimental studies on condensation of zeotropic mixtures in tubes.

Author/source	Tube type	Operating conditions
Berrada et al. [8]	Horizontal smooth tube: 8.92 mm	R22, R134a, R134a/R23 (93/7, 90/10, 86/14 M%) m = 80–480 kg/(m^2 s), q = 2–50 kW/m^2, x = 0.01–∼ 0.80
Shao et al. [9]	Horizontal smooth tube: 6 mm	R32, R134a, R32/ R134a (26.5/73.5, 55/45, 74.5/23.5 mass%) T_{sat} = 23–40 °C, m = 131–369 kg/(m^2 s), q = 4–15 kW/m^2, x = 0.10–0.95
Shao et al. [10,11]	Horizontal smooth tube: 6 mm	Pure and azeotropic fluids: R12, R22, R134a, R502 Non-azeotropic mixtures: R404A, R407C, R32/R134a m = 150–450 kg/(m^2 s), x = 0.11–0.97
Eckels et al. [12]	Horizontal smooth tube: 8 mm	R22, R32/ R125 (45/55, 25/75 M%) m = 130–400 kg/(m^2 s), x = 0.15–0.85
Smit et al. [13]	Horizontal smooth tube: 8.11 mm	R22/R142b (from 90/10 to 50/50 mass%) P = 2.43 MPa, m = 40–800 kg/(m^2 s), x = 0.10–0.90
Huang et al. [14–17]	Horizontal smooth tube: 1.6, 4.8 mm Horizontal microfin tube: 4, 5 mm	R410A-oil (oil concentrations from 0% to 5%) m = 200–600 kg/(m^2 s), x = 0.20–0.90
Thonon et al. [18]	Compact plate heat exchanger	Pentane, butane, propane, butane/propane (49/51, 28/72 M%) P = 0.15–1.8 MPa, Re_{lo} = 100–2000
Macdonald et al. [19]	Horizontal smooth tube: 7.75, 14.45 mm	Ethane/propane (33/67, 67/33 M%) P/P_{cr} = 0.46–0.67, m = 150, 300, 450 kg/(m^2 s), x = 0.05–0.95
Neeraas [20]	Upward flow in coil-wound tube D = 2 m, d = 10 mm, β=10°	Ethane/propane (50/50 M%): P = 3.2–4 MPa, m = 150–300 kg/(m^2 s), x = 0.04–0.98

Table 3
Summary of numerical studies on condensation flow and heat transfer.

Author/source	Model	Tube type	Operating conditions
Sun et al. [26]	New phase-change model	Bubble condensation	Water: $T_{sat} - T_{water}$ = 20 K
Kim et al. [27]	Mass transfer time relaxation parameters	Thermosyphon	Water: T_l = 301.45–373 K, T_v = 373–400 K
Sachin et al. [28]	VOF method Modified Realizable k–ε model	Vertical downflow 10, 20, 43 mm	Water P = 1.5–3.5 atm, flow rate: 0.00857–0.0122 kg/s
Lee et al. [29,30]	VOF method Modified SST k-ω model	Vertical tube Down:11.89 mm Up: 10.16 mm	FC-72 Down: T_{sat} = 58.4–75.0 °C, m = 184–413 kg/(m^2 s) Up: T_{in} = 342.2–345.3 K, m = 58–272 kg/(m^2 s)
Qiu et al. [32]	VOF method Reynolds stress turbulence model	Spiral pipe upflow D = 2 m, d = 10 mm, β=10°	Propane P = 1.2 MPa, m = 150–350 kg/(m^2 s), x = 0.10–0.90
Zhang et al. [34]	Theoretical model	Mini-tube 0.2, 0.5, 1 mm	R410A, R32/125, R32/R134a P = 2.3 MPa, m = 100–700 kg/(m^2 s), x = 0.5–1.0
Deng et al. [35,36]	Non-equilibrium model Mass and heat transfer resistances	Mini-tube 1 mm	Methane/ethane P = 1.0–2.0 MPa, m = 100–300 kg/(m^2 s), q = 6.5–26 kW/m^2, x = 0.25–0.90
Damle et al. [37]	One-dimensional transient model	J-T cryocooler	Nitrogen-hydrocarbons (N_2/CH_4/C_2H_6/C_3H_8/iC_4H_{10}) P = 1.238 MPa, flow rate: 2.64–3.7 kg/s

frictional pressure drop. Boyko's correlation [22] corrected by vapor quality was recommended to calculate heat transfer coefficient of single-component flow while Silver correlations [23,24] corrected by Price-Bell method [25] could satisfactorily predict the mixed effect. The experimental studies mentioned above were summarized in Table 2.

Meanwhile, with the development of computational technology, lots of numerical simulations have been carried out to investigate the condensation flow and heat transfer since its low cost, flexibility and arbitrariness. Sun et al. [26] built a new phase-change model in which the thermal conductivity of saturated phase was forced equal to that of unsaturated phase, whose accuracy was verified by some condensation experiments. Kim et al. [27] discussed mass-transfer time relaxation parameters on evaporation and condensation in a thermosyphon and suggested that the ratio of mass-transfer time relaxation parameters on condensation and evaporation should be equal to liquid-vapor density ratio to ensure mass conservation. Sachin et al. [28] carried out a numerical study on condensation heat transfer and flow pattern in vertical pipes based on volume of fluid (VOF) method. In this simulation, a damping function was considered to solve high velocity gradient at vapor-liquid interface in Realizable k–ε model. Lee et al. [29–30] also considered the turbulence effects in SST k-ω model [31] with a turbulent damping factor of 10 to study the condensation of FC-72 in vertical tubes. Qiu et al. [32] numerically investigated the condensation flow of propane in a spiral tube based on VOF method together with Reynolds stress turbulence model (RSM). In this simulation, the entrainment of vapor-liquid two-phase flow was considered by using Ishii's concentration model [33]. It showed that when the entrainment was considered, the simulated heat transfer coefficient and frictional pressure drop both became smaller, and much closer to experimental results from literatures. Zhang et al. [34] developed a theoretical model and numerically studied the condensation heat transfer of binary mixtures in small horizontal tubes. The results indicated that for the condensation annular flow, there was a maximum interface temperature at a high vapor quality which increased with mass flux. Besides, condensation heat transfer coefficients increased with the concentration of less volatile component in binary mixtures. Deng et al. [35] proposed a model to study condensation heat and mass transfer characteristics of methane/ethane mixtures inside minichannels. In the model, the mass and heat transfer resistances in vapor phase were considered. The results showed that heat and mass transfer resistances in vapor phase both increased with the decreasing mass fluxes and increasing heat fluxes. They also compared the accuracies of equilibrium and non-equilibrium models to predict condensation lengths for binary mixtures and found that non-equilibrium models were better [36]. Damle et al. [37] studied the recuperative heat exchange in a mixed refrigerant J-T cryocooler based on a one-dimensional transient model using different heat transfer correlations. The results demonstrated that the SBG correction method [23,24] could give good predictions of condensation heat transfer coefficients for mixtures with relatively low temperature glide, which was not more than 130 K. The summary of numerical simulations mentioned above was shown in Table 3.

Based on the above analysis, it can be clearly seen that few research efforts have been devoted to the condensation heat transfer and frictional pressure drop characteristics of hydrocarbon mixtures in a spiral tube expect for the study by Neeraas [20]. However, Neeraas [20] only discussed the condensation ethane/propane mixture flow in a spiral pipe at relatively high pressure, but sometimes the actual situation was at lower pressure and also the influence of heat fluxes and inclination angles was not considered. As a result, the accuracies of the correlations which were recommended by Neeraas [20] need to be further discussed under other actual situations (lower pressures, other heat fluxes and other inclination angles) to verify their universal usability.

Consequently, in this paper, a numeral model was established to study condensation flow and heat transfer for hydrocarbon mixtures in a spiral pipe of SWHE while a method was introduced to calculate the mixed effect on heat transfer for hydrocarbon mixtures. Simultaneously, comparing with the experimental data available in Ref. [20] and new flow pattern observation experiments, their accuracy was assessed. Then, it also investigated the characteristics of flow pattern, void fraction, pressure drop and heat transfer for ethane/propane mixture during condensing upward flow in a spiral pipe under the actual conditions (low and high pressures). Finally, comparing with the existing correlations, the better correlations were selected and some important conclusions were drawn.

2. Calculation methods

In the published literatures, the investigation on condensation of hydrocarbon mixtures in upward flow inside a spiral tube was only found in Ref. [20]. Therefore, in order to verify the numerical

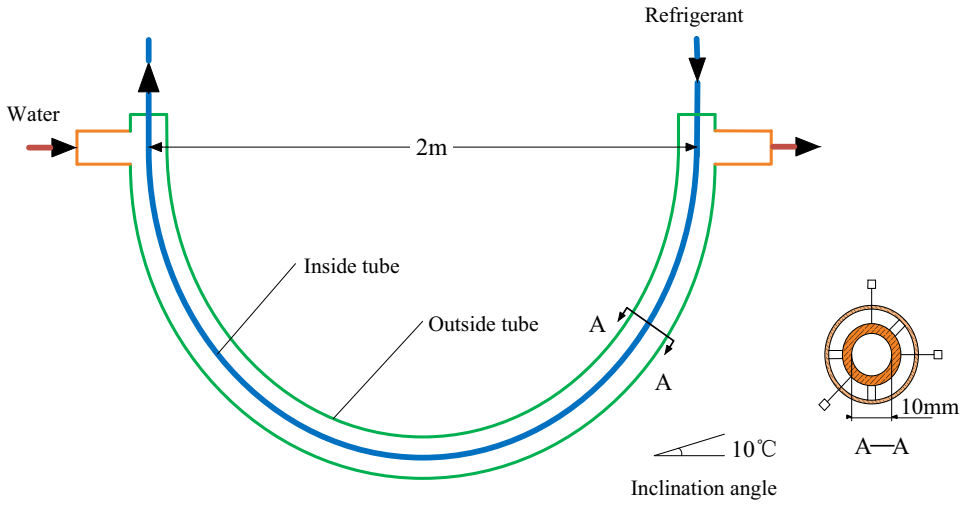

Fig. 2. Experimental model in Ref. [20].

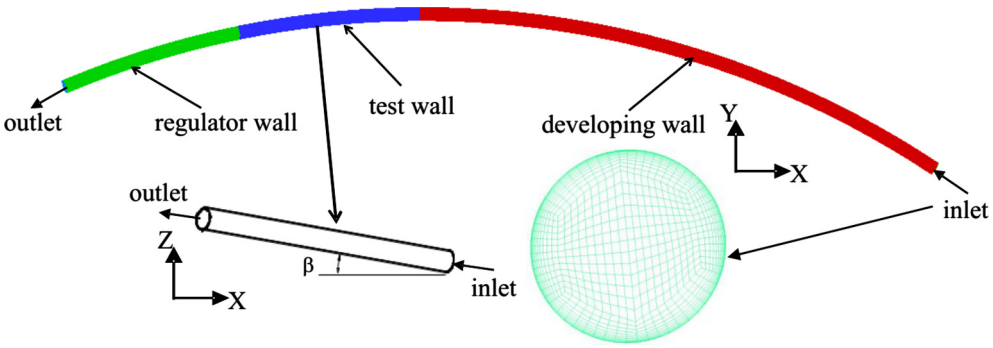

Fig. 3. Computational model and mesh of a spiral pipe.

model in this paper, concurrently considering the calculation accuracy and computational efficiency, a computational model which was simplified from the experimental model in Ref. [20] (as shown in Fig. 2) was established to simulate the condensation heat transfer and pressure drop characteristics for hydrocarbon mixtures upward flow in SWHE tube side, as shown in Fig. 3. The diameter of curvature is 2 m while the hydraulic diameter is 14 mm. The spiral pipe with 6°, 10° and 14° inclination angles in the flow direction has a length of 1 m which contains 0.6 m long section to develop the flow pattern, 0.2 m long section to observe the flow pattern and test the heat transfer coefficient and frictional pressure drop and 0.2 m long section to ensure the stability of pressure measurement. The components of the refrigerant are ethane and propane with molar ratio 1:1.

2.1. Governing equations

For the calculation of condensation multiphase flow in a spiral pipe, the inhomogeneous two-fluid model coupling with thermal phase change model was selected. The Reynolds-averaged governing equations for conservation of mass, momentum, energy, and turbulent quantities can be expressed as follows.

2.1.1. Mass conservation

$$\frac{\partial}{\partial t}(\alpha_l \rho_l) + \nabla \cdot (\alpha_l \rho_l \vec{u}_l) = \Gamma_{lv} \tag{1}$$

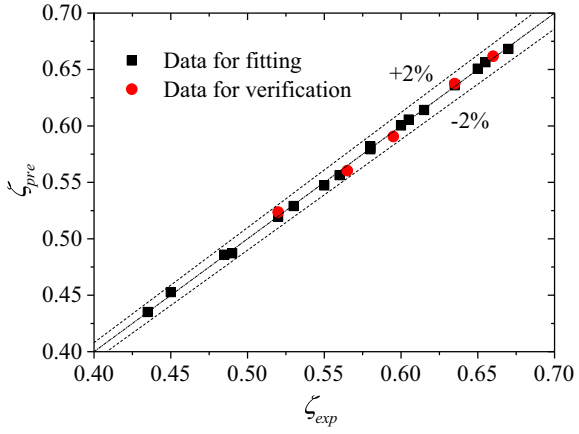

Fig. 4. Comparison between predicted condensation heat ratios by Eq. (6) and experimental ones in Ref. [20].

$$\frac{\partial}{\partial t}(\alpha_v \rho_v) + \nabla \cdot (\alpha_v \rho_v \vec{u}_v) = \Gamma_{vl} \tag{2}$$

where α, ρ and $\vec{u}$ represent the volume fraction, density and velocity, respectively. Subscript l and v denote liquid phase and vapor phase, respectively. Γ_{lv} and Γ_{vl} are the mass flow rate in per unit volume from vapor phase to liquid phase and from liquid phase to vapor phase, respectively; $\Gamma_{lv} = -\Gamma_{vl} = \Gamma^{+}_{lv} - \Gamma^{+}_{vl}$. The term $\Gamma^{+}_{lv} > 0$ represents the positive mass flow rate in per unit volume

from vapor phase to liquid phase. It is important to keep track of the direction of mass transfer process. Γ_{lv} can be expressed as follows:

$$\Gamma_{lv} = \dot{m}_{lv} A_{lv} \tag{3}$$

where A_{lv} is the interfacial area density between liquid phase and vapor phase. $\dot{m}_{lv}$ represents the mass flow rate in per unit interfacial area from vapor phase to liquid phase. It can be calculated based on the thermal phase change model. Besides, the constraint can be also given as $\dot{m}_{lv} = -\dot{m}_{vl}$.

In this paper, vapor phase and liquid phase are both assumed to be continuous phase. The interfacial area density between vapor phase and liquid phase, A_{lv}, can be written as

$$A_{lv} = \frac{\alpha_v \alpha_l}{d_{lv}} \tag{4}$$

where d_{lv} represents the mean interfacial lengths scale between liquid phase and vapor phase, which remarkably influences the heat and mass transfer between the two phase. As heat flux is constant in the wall and mass flux is constant in the spiral pipe, based on energy conservation, d_{lv} has been deduced in our previous study [38], as shown:

$$d_{lv} = \sqrt{\frac{(1-\zeta)\overline{Nu_{lv}}\lambda_{tp}\overline{\alpha_v}\overline{\alpha_l}Ld\gamma_{lv}}{(8|q|Cp_l L\xi + 2m(1-x)Cp_l d\gamma_{lv})\zeta}} \tag{5}$$

where ζ is condensation heat ratio, which characterizes the effective utilization of heat transfer for the condensation, and is defined as the ratio of the latent heat transfer to the total heat transfer; Nu_{lv}, λ_{tp}, γ_{lv} and Cp_l represent Nusselt number between vapor-phase side and liquid-phase side at phase interface, mixture thermal conductivity, latent heat of phase change and specific heat of liquid phase, respectively while m, x, q, d and L denote mass flux, vapor quality and heat flux, hydraulic diameter and length of test section, respectively. In this paper, the simulation results agree well the experimental data from Ref. [20] when ζ is calculated as follows:

$$\zeta = a - b \cdot c^{\left(\frac{\rho_l}{\rho_{tp}}\right)} \tag{6}$$

where a = 0.8704, b = 0.6011, c = 0.8081; it can predict ζ within ±2% error, as shown in Fig. 4.

2.1.2. Momentum conservation

$$\frac{\partial}{\partial t}\left(\alpha_l \rho_l \vec{u}_l\right) + \nabla \cdot \left(\alpha_l \rho_l \vec{u}_l \vec{u}_l\right) = \alpha_l(\rho_l - \rho_{ref})\vec{g} + \nabla \cdot \left\{\alpha_l(\mu_l + \mu_{tl})\left[\nabla \vec{u}_l + (\nabla \vec{u}_l)^T\right]\right\} - \alpha_l \nabla p + \vec{F}_{lv} \tag{7}$$

$$\frac{\partial}{\partial t}\left(\alpha_v \rho_v \vec{u}_v\right) + \nabla \cdot \left(\alpha_v \rho_v \vec{u}_v \vec{u}_v\right) = \alpha_v(\rho_v - \rho_{ref})\vec{g} + \nabla \cdot \left\{\alpha_v(\mu_v + \mu_{tv})\left[\nabla \vec{u}_v + (\nabla \vec{u}_v)^T\right]\right\} - \alpha_v \nabla p + \vec{F}_{vl} \tag{8}$$

where p, μ and μ_t represent pressure, dynamic viscosity and turbulent viscosity, respectively. Subscript *ref* means the reference value, herein, $ref = v$. $\vec{g}$ represents the acceleration of gravity while $\vec{F}_{lv}$ and $\vec{F}_{vl}$ denote the interfacial forces acting on liquid phase due to the presence of vapor phase and on vapor phase due to the presence of liquid phase per unit volume, respectively; $\vec{F}_{lv} = -\vec{F}_{vl}$, they can be calculated as follows:

$$\vec{F}_{lv} = \vec{F}_{D,lv} + \vec{F}_{\sigma,lv} + \left(\Gamma^+_{lv}\vec{u}_v - \Gamma^+_{vl}\vec{u}_l\right) \tag{9}$$

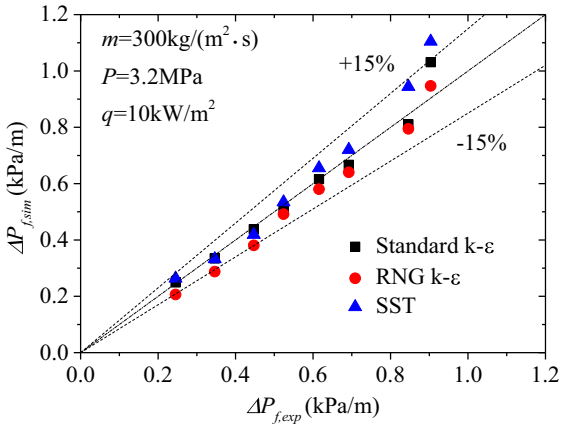

(a) Frictional pressure drop

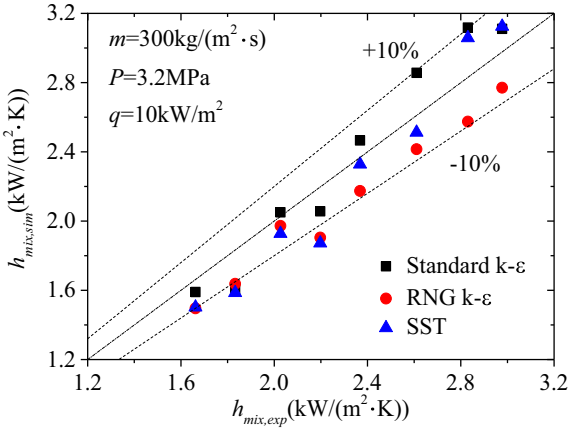

(b) Heat transfer coefficient

Fig. 5. Comparison between simulation values together with modified Silver approach and experimental results in Ref. [20] under different turbulence models.

where $\vec{F}_{D,lv}$ and $\vec{F}_{\sigma,lv}$ mean the drag force and the surface force acting on vapor phase due to the presence of liquid phase per unit volume, respectively; $\left(\Gamma^+_{lv}\vec{u}_v - \Gamma^+_{vl}\vec{u}_l\right)$ means the momentum transfer associated with interphase mass transfer

The drag force $\vec{F}_{D,lv}$ can be modeled as:

$$\vec{F}_{D,lv} = C_D \rho_{tp} A_{lv} \left|\vec{u}_v - \vec{u}_l\right| \left(\vec{u}_v - \vec{u}_l\right) \tag{10}$$

where C_D represents the drag coefficient, C_D = 0.44; ρ_{tp} represents the vapor-liquid mixture density, which can be written as follows:

$$\rho_{tp} = \left(\frac{x}{\rho_v} + \frac{1-x}{\rho_l}\right)^{-1} \tag{11}$$

The surface tension model used in this paper is based on the Continuum Surface Force (CSF) model proposed by Brackbill et al. [39]. It models the surface tension force as a volume force concentrated at the interface, rather than a surface force. And then $\vec{F}_{D,lv}$ can be expressed as follows:

$$\vec{F}_{\sigma,lv} = \dot{f}_{\sigma,lv}\delta_{lv} \tag{12}$$

where

$$\delta_{lv} = |\nabla \alpha_l| \tag{13}$$

$$\dot{f}_{\sigma,lv} = \sigma \kappa_{lv} \vec{n}_{lv} + \nabla_s \sigma \tag{14}$$

where δ_{lv} is the interface delta function; σ is the surface tension coefficient; $\vec{n}_{lv}$ is the interface normal vector pointing from liquid phase to the vapor phase (calculated from the gradient of a smoothed volume fraction); ∇_s is the gradient operator on the interface and κ_{lv} is the surface curvature defined by:

$$k_{lv} = \nabla \cdot \vec{n}_{lv} \tag{15}$$

In order to select the suitable turbulence model, the simulations under different turbulence models (standard k-ε turbulent model, RNG k-ε turbulent model and SST k-ω turbulent model) were carried out when m = 300 kg/(m^2 s), P = 3.2 MPa, x = 0.1–0.87 and q = 10 kW/m^2, as shown in Fig. 5. It indicated that the simulated frictional pressure drop and heat transfer coefficients based on standard k-ε turbulent model have best agreement with experimental results in Ref. [20]. Therefore, in this paper, the standard k-ε turbulent model is selected to use in vapor phase and liquid phase. The turbulent viscosity for vapor phase and liquid phase are both modeled as:

$$\mu_{tv} = C_\mu \rho_v \left(\frac{k_v^2}{\varepsilon_v}\right) \tag{16}$$

$$\mu_{tl} = C_\mu \rho_l \left(\frac{k_l^2}{\varepsilon_l}\right) \tag{17}$$

where C_μ is a constant given as 0.09. k and ε represent turbulent kinetic energy and turbulent dissipation rate respectively. The transport equations for k and ε can be written as follows:

$$\begin{aligned}&\frac{\partial}{\partial t}(\alpha_v \rho_v k_v) + \nabla \cdot (\alpha_v \rho_v \vec{u}_v k_v) \\ &\quad = \nabla \cdot \left[\alpha_v \left(\mu_v + \frac{\mu_{tv}}{\sigma_k}\right) \nabla k_v\right] + \alpha_v (P_{kv} - \rho_v \varepsilon_v) + (\Gamma_{vl}^+ k_l - \Gamma_{lv}^+ k_v)\end{aligned} \tag{18}$$

$$\begin{aligned}&\frac{\partial}{\partial t}(\alpha_v \rho_v \varepsilon_v) + \nabla \cdot (\alpha_v \rho_v \vec{u}_v \varepsilon_v) \\ &\quad = \nabla \cdot \left[\alpha_v \left(\mu_v + \frac{\mu_{tv}}{\sigma_\varepsilon}\right) \nabla \varepsilon_v\right] + \alpha_v \frac{\varepsilon_v}{k_v} (C_{\varepsilon 1} P_{kv} - C_{\varepsilon 2} \rho_v \varepsilon_v) \\ &\quad + (\Gamma_{vl}^+ \varepsilon_l - \Gamma_{lv}^+ \varepsilon_v)\end{aligned} \tag{19}$$

$$\begin{aligned}&\frac{\partial}{\partial t}(\alpha_l \rho_l k_l) + \nabla \cdot (\alpha_l \rho_l \vec{u}_l k_l) \\ &\quad = \nabla \cdot \left[\alpha_l \left(\mu_l + \frac{\mu_{tl}}{\sigma_k}\right) \nabla k_l\right] + \alpha_l (P_{kl} - \rho_l \varepsilon_l) + (\Gamma_{lv}^+ k_v - \Gamma_{vl}^+ k_l)\end{aligned} \tag{20}$$

$$\begin{aligned}&\frac{\partial}{\partial t}(\alpha_l \rho_l \varepsilon_l) + \nabla \cdot (\alpha_l \rho_l \vec{u}_l \varepsilon_l) \\ &\quad = \nabla \cdot \left[\alpha_l \left(\mu_l + \frac{\mu_{tl}}{\sigma_\varepsilon}\right) \nabla \varepsilon_l\right] + \alpha_l \frac{\varepsilon_l}{k_l} (C_{\varepsilon 1} P_{kl} - C_{\varepsilon 2} \rho_l \varepsilon_l) + (\Gamma_{lv}^+ \varepsilon_v - \Gamma_{vl}^+ \varepsilon_l)\end{aligned} \tag{21}$$

where $C_{\varepsilon 1}$, $C_{\varepsilon 2}$, σ_k and σ_ε are constant with the values of 1.44, 1.92, 1.3 and 1.0, respectively. P_k is the turbulence production due to viscous and buoyancy forces, modeled as follows:

$$P_{ki} = \mu_t \nabla \vec{u}_i \cdot (\nabla \vec{u}_i + \nabla \vec{u}_i^T) - \frac{2}{3} \nabla \cdot \vec{u}_i (3\mu_{ti} \nabla \cdot \vec{u}_i + \rho_i k_i) + P_{kbi} \tag{22}$$

where P_{kbi} is the buoyancy production term and can be written for the full buoyancy model as

$$P_{kbi} = -\frac{\mu_{ti}}{\rho_i} g \cdot \nabla \rho_i \tag{23}$$

where subscript i means any phase, herein, $i = v$ or l.

2.1.3. Energy conservation

$$\frac{\partial}{\partial t}(\alpha_v \rho_v \gamma_v) + \nabla \cdot (\alpha_v \rho_v \vec{u}_v \gamma_v) = \nabla \cdot (\alpha_v \lambda_v \nabla T_v) + Q_v \tag{24}$$

$$\frac{\partial}{\partial t}(\alpha_l \rho_l \gamma_l) + \nabla \cdot (\alpha_l \rho_l \vec{u}_l \gamma_l) = \nabla \cdot (\alpha_l \lambda_l \nabla T_l) + Q_l \tag{25}$$

where γ, λ and T represent the enthalpy, thermal conductivity and temperature, respectively. Q_v and Q_l denote total interphase heat transfer to vapor phase across the interface with liquid phase and to liquid phase across the interface with vapor phase, respectively, $Q_v = -Q_l$. Based on the thermal phase change model, they can be written as follows:

$$Q_v = q_v + \Gamma_{vl} \gamma_{vS} \tag{26}$$

$$Q_l = q_l + \Gamma_{lv} \gamma_{lS} \tag{27}$$

where q_v and q_l denote the sensible interphase heat transfer to vapor phase across the interface with liquid phase and to liquid phase across the interface with vapor phase, respectively. γ_{vS} and γ_{lS} represent interfacial values of enthalpy carried into vapor phase and liquid phase due to phase change, respectively. $\Gamma_{vl}\gamma_{vS}$ and $\Gamma_{lv}\gamma_{lS}$ represent heat transfer induced by interphase mass transfer into vapor phase from liquid phase and into liquid phase from vapor phase, respectively. Then, their relation can be given as

$$q_v + q_l = -(\Gamma_{vl}\gamma_{vS} + \Gamma_{lv}\gamma_{lS}) \tag{28}$$

Substituting Eq. (3) into Eq. (28), $\dot{m}_{lv}$ is given as

$$\dot{m}_{lv} = \frac{q_v + q_l}{A_{lv}(\gamma_{vS} - \gamma_{lS})} \tag{29}$$

Meanwhile

$$\begin{aligned}&\dot{m}_{lv} > 0 \Rightarrow \gamma_{lS} = \gamma_{lsat}, \gamma_{vS} = \gamma_v \\ &\dot{m}_{lv} < 0 \Rightarrow \gamma_{lS} = \gamma_l, \gamma_{vS} = \gamma_{vsat}\end{aligned} \tag{30}$$

Based on the two resistance model, q_v and q_l can be expressed as, respectively.

$$q_l = h_l A_{lv} (T_S - T_l) \tag{31}$$

$$q_v = h_v A_{lv} (T_S - T_v) \tag{32}$$

where h_v and h_l respectively represent the heat transfer coefficient of liquid phase and vapor phase on one side of phase interface between vapor phase and liquid phase. T_S is the interfacial temperature, which can be determined from considerations of thermodynamic equilibrium. Ignoring the effects of surface tension on pressure, the interfacial temperature can be written as

$$T_S = T_{sat} \tag{33}$$

where T_{sat} represents the saturation temperature. For mixtures, T_{sat} is determined by the given pressure and vapor quality; in this paper, it is assumed as constant due to the relatively small changes of pressure and vapor quality.

In the simulation, it ignores the temperature difference in the vapor core among different components and the degree of supercooling is very slight for vapor phase in the condensation flow. Therefore, for the vapor phase on one side of the phase interface, a zero resistance condition is adopted in this paper. This is equivalent to an infinite heat transfer coefficient in vapor phase side of the phase interface, $h_v = \infty$. Its effect is to force the interfacial temperature to be the same as the vapor phase temperature, as shown here,

$$T_S = T_v \tag{34}$$

Table 4
The test of grid-independent validation (m = 300 kg/(m^2 s), P = 3.0 MPa, q = 10 KW/m^2, x = 0.869).

Grid label	Grid amount $\times 10^4$	Frictional pressure drop kPa/m	Amount of change %	Film Heat transfer coefficient kW/(m^2 K)	Amount of change %
No. 1	40.60	1.239		3.765	
No. 2	60.16	1.186	−4.27	3.984	5.82
No. 3	85.40	1.175	−0.93	4.028	1.01

Table 5
Temperature glide of the ethane/propane mixture (molar ratio 1:1).

Pressure MPa	Bubble temperature K	Dew temperature K	Temperature glide K
2.0	291.77	306.36	14.59
3.0	311.93	323.68	11.75
3.2	315.39	326.53	11.14
3.8	325.00	334.16	9.16

Further, according to the mixture model and the two resistance model, the following equations can be gotten.

$$h_{lv} = \lambda_{tp} Nu_{lv}/d_{lv} \tag{35}$$

$$\frac{1}{h_{lv}} = \frac{1}{h_l} + \frac{1}{h_v} \tag{36}$$

where h_{lv} represents the heat transfer coefficient between vapor phase side and liquid phase side.

Then, considering $h_v = \infty$, the heat transfer coefficient h_l can be written as

$$h_l = \lambda_{tp} Nu_{lv}/d_{lv} \tag{37}$$

2.2. Numerical schemes

The characteristics of flow pattern, void fraction, heat transfer and pressure drop for ethane/propane mixture during condensing upward flow in a spiral pipe was simulated using ANSYS CFX. The fluid domain was meshed with hexahedral grid, meanwhile, with fine meshes near the wall, as shown in Fig. 3. Three different meshes were performed in simulation, as shown in Table 4. The amount of change means the relatively change of the values with the increase of mesh amount. The results became mesh-independent when the mesh amount reached 601,600 elements. Therefore, the mesh which comprised of 601,600 elements was used in the present study, a decision made in consideration of grid-independent and computation efficiency. The Reynolds-averaged Navier-Stokes equations were integrated over each control volume, so that the relevant quantities (such as energy and momentum and mass) were conserved in each control volume. Discrete conservation equations in a form of linear set of equations were obtained by applying Finite Volume Method based on Finite Element Method. The central deferential scheme was applied to treat the diffusion terms. The convection terms were treated applying the high resolution scheme, which was second-order accurate. The inhomogeneous two-fluid model together with standard k-ε turbulence model and thermal phase change model was adopted while the scalable wall function was selected to calculate the flow near the wall. The mass flow, vapor volume fraction and temperature were adopted at inlet. The static pressure was used at outlet and the constant heat flux was considered in the wall of spiral pipe. All physical properties of hydrocarbon mixtures were computed from REFPROP [40]. The temperature glide of ethane/propane mixture in this study is shown in Table 5. It can be clearly seen that for all given saturation pressure, the temperature glides are all less than 15 K, which indicates that the ethane/propane mixture using in this study always belongs to mixtures with relatively low temperature glide defined in Ref. [37] and the SBG correction method [23,24] can be used to predict the mixture effect of hydrocarbon mixtures in this paper. The detailed calculation approach is shown as follows.

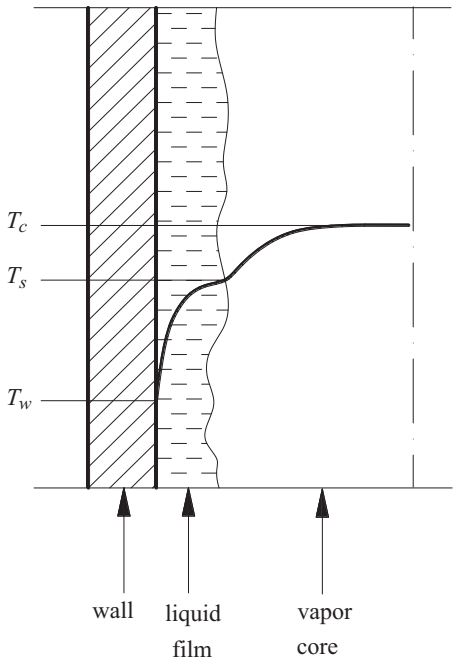

Fig. 6. Schematic of condensing process of refrigerant mixture.

3. Calculation model of condensation heat transfer coefficient for refrigerant mixture

The condensing process of refrigerant mixture in tubes is shown in Fig. 6. It is clearly seen that the condensation heat transfer coefficient for refrigerant mixture can be generally predicted as follows.

The total heat flux through liquid film can be given by

$$q_{tot} = h_{film} \cdot (T_S - T_w) \tag{38}$$

It can be also obtained as:

$$q_{tot} = h_{mix} \cdot (T_c - T_w) \tag{39}$$

The heat flux due to heat and mass transfer through vapor core can be calculated as:

$$q_{core} = h_{core} \cdot (T_c - T_S) \tag{40}$$

where h_{film}, h_{core} and h_{mix} represent liquid film, vapor core and mixed heat transfer coefficient, respectively. T_s, T_c and T_w represent interfacial, vapor core and wall temperature, respectively.

Combining Eqs. (38)–(40), it can get

$$\frac{1}{h_{mix}} = \frac{1}{h_{film}} + \left(\frac{q_{core}}{q_{tot}}\right)\left(\frac{1}{h_{core}}\right) \tag{41}$$

According to Eq. (41), it is clearly shown that h_{mix} is closely related to h_{film}, h_{core} and q_{core}/q_{tot}. h_{film} can be calculated by using a single-component two-phase heat transfer coefficient model.

For the calculation of h_{core} and q_{core}/q_{tot}, the Silver approach [23,24] has been widely used. They defined h_{core} as the smooth gas superficial single-phase heat transfer coefficient h'_v, neglecting the effects of two-phase enhancement at the interface and mass transfer on vapor-phase heat transfer. h'_v can be calculated as:

$$h_{core} = h'_v = 0.021\frac{\lambda_v}{d-2\delta}\left(\frac{mxd}{\mu_l\alpha_v^{0.5}}\right)^{0.8} Pr_v^{0.43} \tag{42}$$

where δ is the liquid film thickness, $\delta = 0.5\,(1-\alpha_v^{0.5})d$.

The ratio between sensible to total heat flux Z can be calculated as:

$$Z = \frac{q_{core}}{q_{tot}} = x\cdot Cp_v\left(\frac{d}{d-2\delta}\right)\frac{dT}{d\gamma} \tag{43}$$

where $dT/d\gamma$ is the ratio between temperature and enthalpy, which can be obtained from the temperature-enthalpy curve for refrigerant mixture.

Then

$$h_{mix} = \frac{h_{film}}{1+h_{film}\Phi} \tag{44}$$

where

$$\Phi = \frac{Z}{h_{core}} \tag{45}$$

where Φ is heat and mass transfer resistance in vapor core for mixture.

The tests on condensation heat transfer coefficients for propane/ethane mixtures from Ref. [20] by Neeraas showed that the Silver approach could obviously affect the prediction of heat transfer coefficients for mixtures, but there was still insufficient, and in some cases, the errors using this method were still too large. Neeraas suggested that the large errors were mainly caused by the two simplified assumptions in the calculation of h_{core}, so Neeraas introduced C_f and θ to modify the calculation of h_{core}, as shown here:

$$h_{core} = h'_v C_f \theta \tag{46}$$

where C_f represents the effect of two-phase enhancement at interface which can be obtained by Price-Bell method [25] while θ represents the effect of mass transfer which can be calculated by Sardesai's correlation [41]. Their concrete forms are shown as follows:

$$C_f = \left[(dp/dl)_{tp}^{fric}/(dp/dl)_v^{fric}\right]^{0.445} \tag{47}$$

$$\theta = \frac{a}{e^a-1} \tag{48}$$

where

$$a = \frac{qc_{pv}}{\gamma_{lv}h'_vC_f} \tag{49}$$

In this paper, the above method is named as modified Silver approach. The modified Silver approach together with Boyko's correlation could be used to predict the condensation heat transfer coefficient for propane/ethane mixtures from Ref. [20].

Therefore, in this paper, for the calculation of condensation heat transfer coefficient for refrigerant mixture, the following method were used.

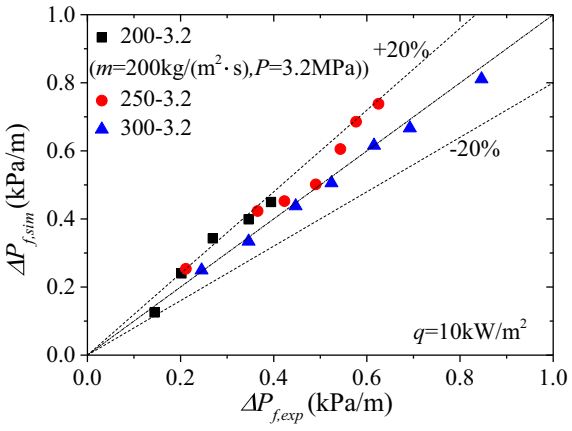

(a) Frictional pressure drop

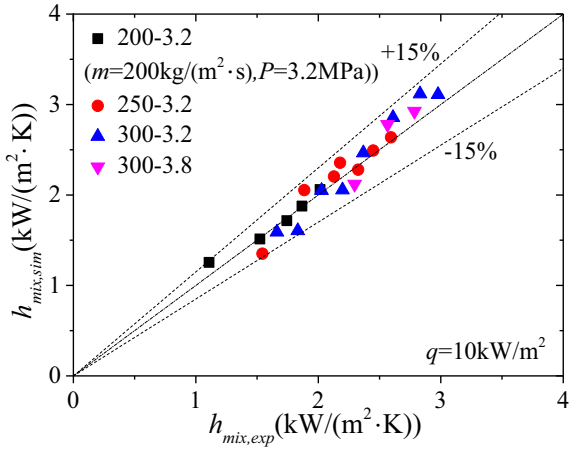

(b) Heat transfer coefficient

Fig. 7. Comparison between simulation values together with modified Silver approach and experimental results in Ref. [20] under different operating parameters.

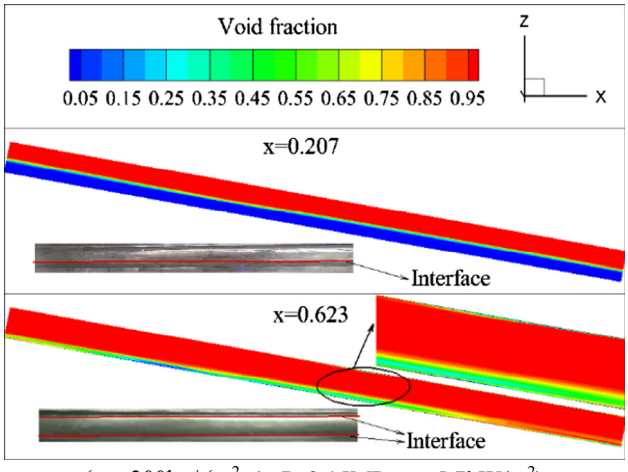

(*m*= 300kg/ (m²·s), *P*=3.15MPa, *q*=5.7kW/m²)

Fig. 8. Comparison between simulated flow patterns with experimental ones under different vapor qualities.

(1) Taking the refrigerant mixture as single-component fluid when the averaged physical properties are used without considering the influence of mixed effects on heat transfer,

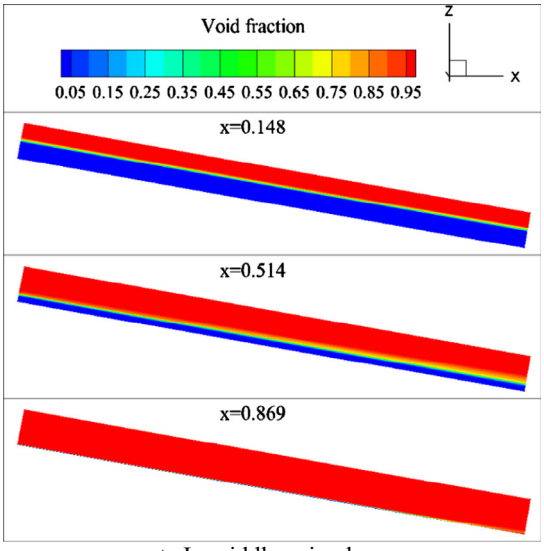

Fig. 9. Void fraction of three typical flow patterns from this study.

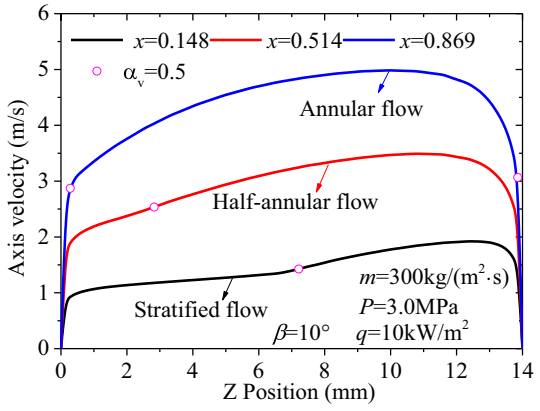

Fig. 10. Velocity profile of three typical flow patterns from this study.

the condensation heat transfer coefficient (h_{film}) of quasi-pure working fluid can be calculated by simulations using the calculation method established in Section 2 in this paper.

(2) Using the modified Silver approach to calculate the mixed effect on heat transfer, the condensation heat transfer coefficient (h_{mix}) for refrigerant mixture can be obtained.

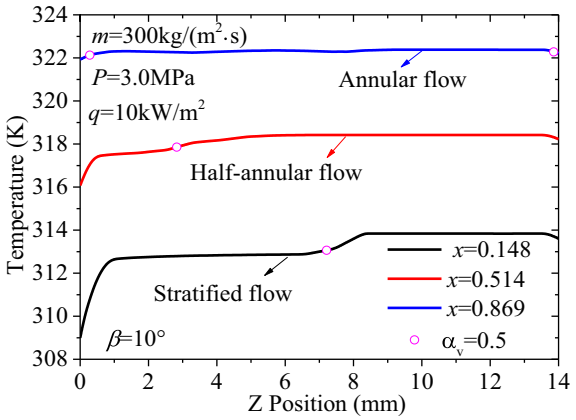

Fig. 11. Temperature profile of three typical flow patterns from this study.

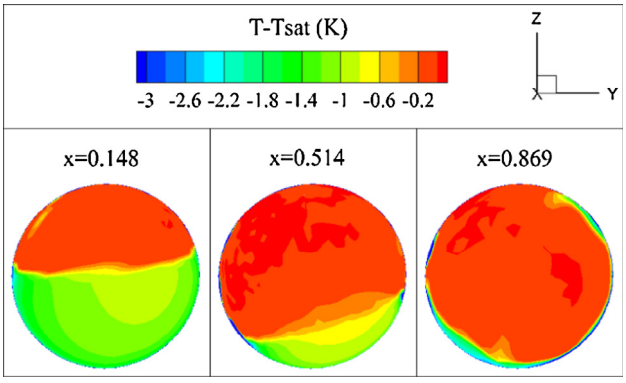

Fig. 12. Super-cooling temperature field of three typical flow patterns from this study.

4. Results and discussion

4.1. Comparison between simulation results and experimental data

In order to validate the model used in this paper, the simulations on the condensation heat transfer and pressure drop characteristics for ethane/propane mixture upward flow in a spiral pipe were carried out to compare with experimental results in Ref. [20] when m = 200, 250, 300 kg/(m^2 s), P = 3.2, 3.8 MPa, x = 0.1–0.90 and q = 10 kW/m^2, as shown in Fig. 7. It indicates that the deviations of frictional pressure drop and heat transfer coefficients between simulation values together with modified Silver approach and experimental results in Ref. [20] are within ±20% and ±15% respectively under different operating parameters. Therefore, the model can be used to study the condensation heat transfer and pressure drop characteristics for ethane/propane mixture upward flow in a spiral pipe.

Meanwhile, the ability of the model to approximately predict flow patterns in a spiral pipe can be verified by flow pattern observation experiments based on an experimental rig, which was set up by our research group members. The experimental apparatus was introduced in their previous investigations [42]. In this study, the only difference was that two flow pattern observation windows were arranged before the entrance and after the exit of the tube side. Then, two flow pattern observation experiments and corresponding simulations were both performed for methane/propane

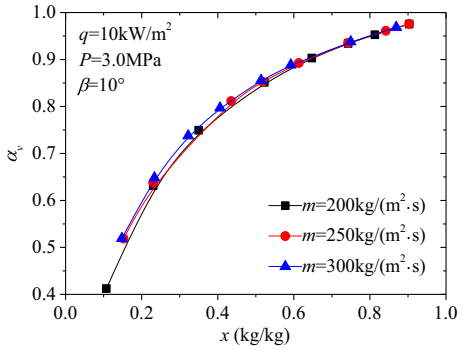

(a) Under different mass fluxes

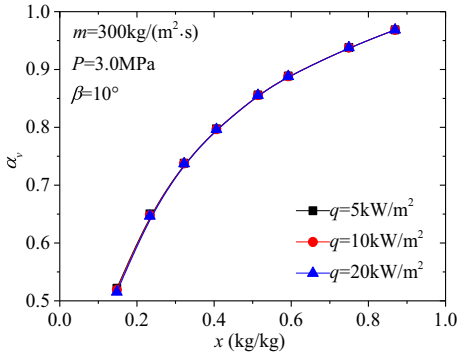

(b) Under different heat fluxes

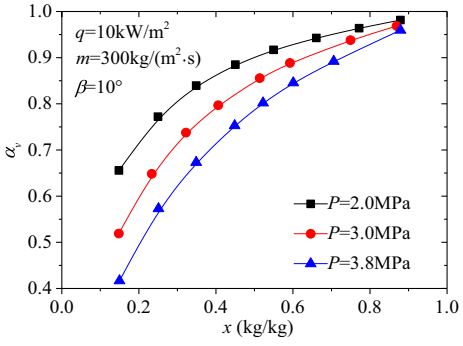

(c) Under different saturation pressure

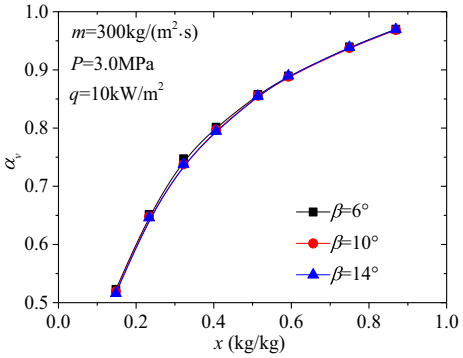

(d) Under different inclination angles

Fig. 13. Void fraction vs. vapor quality under different parameters.

mixture with molar ratio 66:34 when m = 300 kg/(m^2 s), P = 3.15 MPa, x = 0.207, 0.623 and q = 5.7 kW/m^2. The comparison between the experimental flow patterns and simulation results is given in Fig. 8. It shows that the simulated flow patterns coincide with experimental ones, which indicates that the model can be used to predict flow patterns in a spiral pipe.

4.2. Characteristics of condensation flow pattern and void fraction

Firstly, the characteristics of condensation flow pattern and void fraction for ethane/propane upward flow in a spiral pipe are discussed when mass flux, heat flux, saturation pressure, inclination angle and vapor quality are from 200 to 300 kg/(m^2 s), 5 to 20 kW/m^2, 2.0 to 3.8 MPa, 6° to 14° and 0.1 to 0.9, respectively.

As known, different parameters may lead to different flow patterns. In this study, three typical flow patterns (stratified flow, half-annular flow and annular flow) are observed, as shown in Fig. 9. It describes void fraction in the middle axis-plane and cross-plane of test section where m = 300 kg/(m^2 s), P = 3.0 MPa, q = 10 kW/m^2, β = 10° and x = 0.148, 0.514 and 0.869, respectively. Meanwhile, Figs. 10 and 11 give out the velocity and temperature profiles in vertical center line of the middle cross-plane of test section, respectively; the circle in Figs. 10 and 11 is the location of vapor-liquid interface (void fraction is equal to 0.5). Besides, Fig. 12 describes the super-cooling temperature field in the middle cross-plane of test section for the three typical flow patterns in this study.

From Figs. 9 and 10, it is concluded that with the increase of vapor quality, the thickness of liquid film near the wall becomes thinned while the velocity and vapor-liquid velocity ratio both increase; the flow pattern is transformed from stratified flow into half-annular flow and then converted into annular flow. In the stratified flow (Fig. 9B(a)), the flow is mainly affect by gravitational force, liquid phase is mainly located at the bottom of the pipe as a result of higher density. In the half-annular (Fig. 9B(b)), the gravity effect decreases while the shear effect of vapor phase increases, leading to liquid phase spreading from the bottom to the wall of the pipe, but the complete circle has not formed; simultaneously, the vapor–liquid interface tilts because of obvious centrifugal force in the spiral pipe. In the annular flow (Fig. 9B(c)), the shear effect of vapor phase is the main force of the flow, liquid phase is almost evenly distributed near the wall of the tube.

Fig. 11 states that in the stratified flow, that temperature profile has a big transilience from liquid phase to vapor phase, but it slightly changes in half-annular and annular flow. Meanwhile, the temperature gradient near the wall is maximum in stratified flow, followed by in half-annular flow, smallest in annular flow, resulting in best heat transfer in annular flow, followed by in half-annular flow, worst in stratified flow.

Fig. 12 illustrates that for the different flow patterns, the super-cooling temperature distributions are related to the liquid film thickness. With the decrease of liquid film thickness (the increase of vapor quality), the super-cooling temperature distributions will become symmetrical while the average the super-cooling temperature will become smaller, leading better heat transfer.

Fig. 13 presents the void fraction varies with vapor quality under different parameters. It shows the continuous increase with vapor quality but the increase rate becomes slow under different parameters. This is because the vapor has occupied most space of

Table 6
Description of correlation for void fraction.

Authors	Void fraction correlation
Steiner [44]	$\alpha_v = \frac{x}{\rho_v}\left\{[1+0.12(1-x)]\left[\frac{x}{\rho_v}+\frac{1-x}{\rho_l}\right]+\frac{1.18(1-x)[g\sigma(\rho_l-\rho_v)]^{0.25}}{m\rho_l^{0.5}}\right\}^{-1}$
Chisholm [45]	$\alpha_v = \left[1+\left(1-x+x\frac{\rho_l}{\rho_v}\right)^{0.5}\left(\frac{1-x}{x}\right)\left(\frac{\rho_v}{\rho_l}\right)\right]^{-1}$
Zivi [46]	$\alpha_v = \left[1+\left(\frac{1-x}{x}\right)\left(\frac{\rho_v}{\rho_l}\right)^{0.67}\right]^{-1}$
Baroczy [47]	$\alpha_v = \left[1+\left(\frac{1-x}{x}\right)^{0.74}\left(\frac{\rho_v}{\rho_l}\right)^{0.65}\left(\frac{\mu_l}{\mu_v}\right)^{0.13}\right]^{-1}$

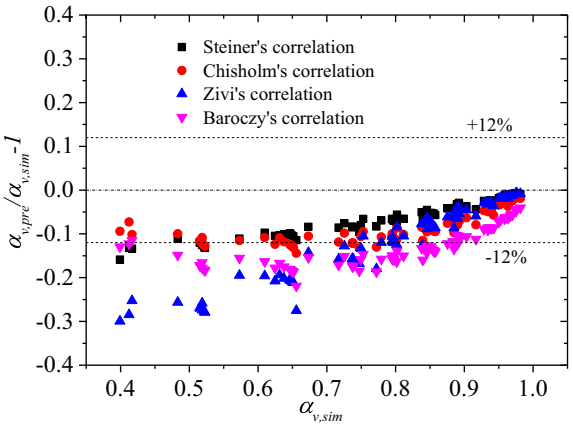

Fig. 14. Void fraction: comparison between existing correlations and simulation results.

Table 7
ARD, MARD and percentage within ±12% error for the existing void fraction correlations.

Correlation	ARD	MARD	Percentage within ±12%
Steiner [44]	−6.08%	6.08%	92.39%
Chisholm [45]	−8.25%	8.25%	82.61%
Zivi [46]	−10.82%	10.82%	64.13%
Baroczy [47]	−12.78%	12.78%	35.87%

the pipe when vapor quality becomes large enough, so to further increase vapor quality, the void fraction slowly changes. Besides, Fig. 13(a) indicates that the void fraction slightly increases as the mass flux increases, just because with the increasing mass flux, the real liquid velocity increases more quickly than the real vapor velocity, resulting in the decrease of vapor-liquid velocity ratio; Further, From Fig. 13(b) and (c), it is found that heat flux has little influence on the void fraction while as saturation pressure decreases, the void fraction obviously increases due to the increase of liquid-vapor density ratio. It can be seen from Fig. 13(d) that the effect of inclination angle on void fraction is insignificant.

An appropriate void fraction correlation is needed to calculate the accelerated pressure drop in the two-phase flow. However, different void fraction correlations have different accuracies for different experiments [43], so their applicability to predict void fraction for ethane/propane mixture upward flow in a spiral pipe should be assessed. The void fraction correlations used in this paper were listed in Table 6. We chose the average deviation (ARD) and mean absolute deviation (MARD) to evaluate void fraction correlations. They are defined as follows:

$$\mathrm{ARD} = \frac{1}{N}\sum_{i=1}^{N}\left(\frac{\text{Predicted value}_i}{\text{Simulated value}_i} - 1\right) \times 100\% \tag{50}$$

$$\mathrm{MARD} = \frac{1}{n}\sum_{i=1}^{n}\left|\frac{\text{predicted value}_i}{\text{simulated value}_i} - 1\right| \times 100\% \tag{51}$$

The comparisons between the above void fraction correlations and simulation results are shown in Fig. 14. The results indicate that the deviations for all void fraction correlations are always negative and gradually decrease with the increasing void fraction. Their ARD, MARD and percentage of data points correctly predicted simulation cases within ± 12% error are given in Table 7. It is clearly seen that Steiner's correlation has the best coincidence with simulation results, and the deviations are almost within ±12%.

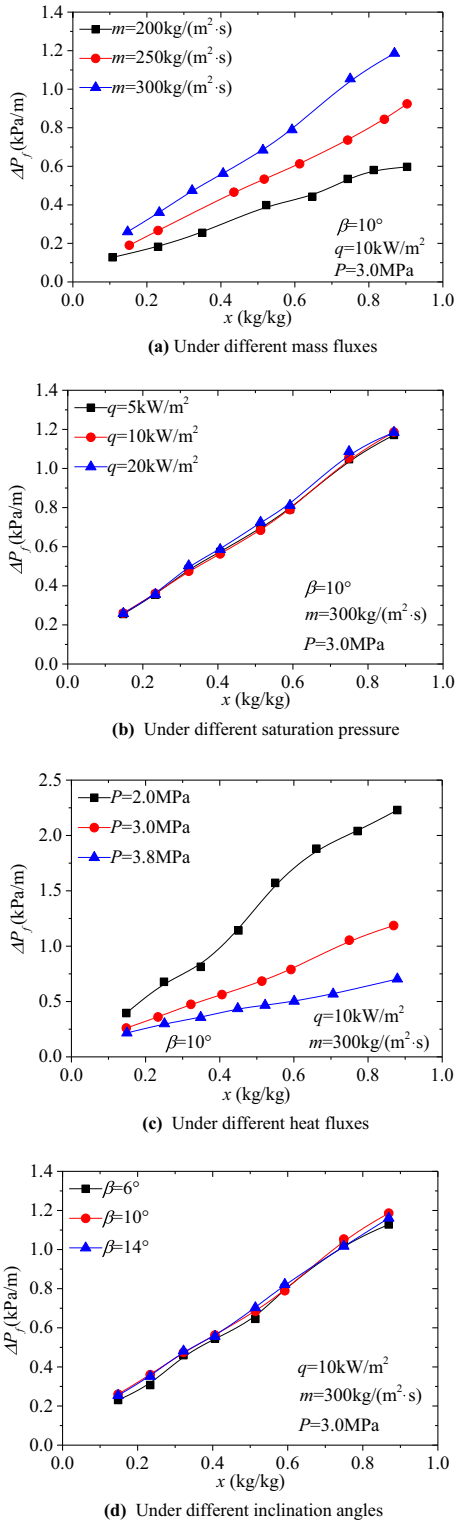

Fig. 15. Frictional pressure drop vs. vapor quality under different parameters.

Therefore, Steiner's correlation can be used to predict void fraction characteristics for ethane/propane mixture upward flow in a spiral pipe.

4.3. Characteristics of condensation pressure drop

The characteristics of condensation pressure drop for ethane/propane mixture upward flow in a spiral pipe are discussed as follows when mass flux, heat flux, saturation pressure, inclination

Table 8
Description of correlation for frictional pressure drop.

Authors	Frictional pressure drop correlation
Darcy and Weisbach [50]	$\left(\frac{dp}{dl}\right)_f = f\frac{\rho}{2}\frac{u^2}{d}$, $f = f_s = \frac{0.3164}{Re^{0.25}}$
Gnielinski [51]	$f = f_c = f_s + 0.03\left(\frac{d}{D}\right)^{0.5}$
Friedel [48]	$\left(\frac{dp}{dl}\right)_{tp} = \Phi_{l0}^2\left(\frac{dp}{dl}\right)_{l0}$, $\phi_{l0}^2 = E + \frac{3.23\cdot F\cdot H}{Fr_{tp}^{0.045}We_{tp}^{0.035}}$ $E = (1-x)^2 + \frac{x^2\cdot\rho_l f_{v0}}{\rho_v f_{l0}}$, $Fr_{tp} = \frac{m^2}{gd\rho_{tp}^2}$, $We_{tp} = \frac{m^2 d}{\sigma\rho_{tp}}$ $F = x^{0.78}(1-x)^{0.224}$, $H = \left(\frac{\rho_v}{\rho_l}\right)^{0.91}\left(\frac{\mu_v}{\mu_l}\right)^{0.19}\left(1-\frac{\mu_v}{\mu_l}\right)^{0.7}$
Carter [49]	$\phi_{l0}^2 = 1 + \frac{\rho_l}{\rho_v}\cdot x^{(1+5.52/P)}\cdot e^{(1-x)} - \left(\frac{x}{0.9}\right)^{\left(\frac{9.75}{P}\right)}\frac{f_c}{f_s} = 1.1 - 0.028\Big/\left[Re_{l0}\left(\frac{d}{D}\right)^2\right]$
Fuchs [21]	$\left(\frac{dp}{dl}\right)_{tp} = \left(\frac{dp}{dl}\right)_{l0} + \varphi_{1v}\left[\left(\frac{dp}{dl}\right)_{v0} - \left(\frac{dp}{dl}\right)_{l0}\right]$ $\varphi_{1v} = \sum_{i=1}^{n} C_i\left(Fr_{l0}, \frac{\rho_l}{\rho_v}\right)\cdot x^{i-1}$
Neeraas (Modified Fuchs) [20]	$\varphi'_{1v} = \varphi_{1v}\left\{1.0 - \left[1.0 - 0.3\cdot g\left(\frac{\rho_l}{\rho_v}\right)\right]\cdot h(x)\right\}$ $h(x) = \begin{cases} \frac{\sin(\pi x)+\sin(\pi x^3)}{1.69}, & x \leqslant 0.725 \\ 1.0 - \sin\left[\frac{\pi}{2}\left(\frac{x-0.725}{0.275}\right)^{5\cdot x^{3.5}}\right], & x > 0.725 \end{cases}$ $g\left(\frac{\rho_l}{\rho_v}\right) = \begin{cases} 6.5^{0.4}, & \frac{\rho_l}{\rho_v} \leqslant 6.5 \\ \left(\frac{\rho_l}{\rho_v}\right)^{0.4}, & 6.5 < \frac{\rho_l}{\rho_v} \leqslant 20 \\ \frac{1.0}{0.3}, & \frac{\rho_l}{\rho_v} > 20 \end{cases}$

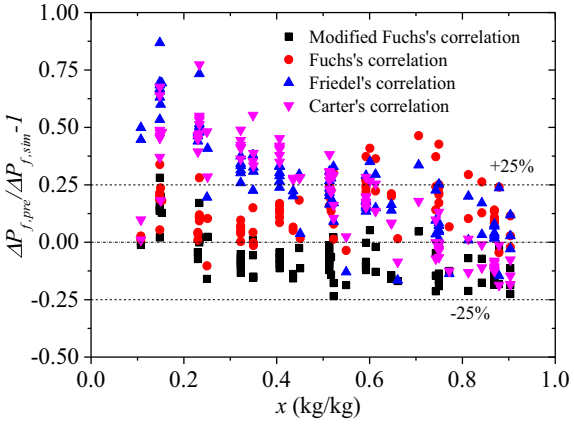

Fig. 16. Frictional pressure drop: comparison between the existing correlations and simulation results.

Table 9
ARD, MARD and percentage within ±25% error for above two-phase frictional pressure drop correlations.

Correlation	ARD	MARD	Percentage within ±25%
Modified Fuchs [20]	−6.85%	10.67%	98.91%
Fuchs [21]	15.23%	15.71%	83.70%
Carter [49]	22.64%	26.86%	46.74%
Friedel [48]	26.25%	27.57%	51.09%

angle and vapor quality are from 200 to 300 kg/(m^2 s), 5 to 20 kW/m^2, 2.0 to 3.8 MPa, 6° to 14° and 0.1 to 0.9, respectively.

The frictional pressure drop under different parameters is plotted versus with vapor quality in Fig. 15. It increases continuously with vapor quality but the increasing rate becomes slow under different parameters; this is because with the increase of vapor quality, the vapor-liquid velocity ratio increases and then the vapor-liquid shear force and the shear force between liquid film and wall both enhance. Besides, Fig. 15(a) shows that the frictional pressure drop significantly increases as mass flux increases especially at high vapor quality; just because with the increasing mass flux, the velocity increases leading the enhancement of shear force between liquid film and wall. At the same time, Fig. 15(b) states that the frictional pressure drop does not almost change with the increasing heat flux since it has little influence on vapor-liquid distribution. Further, Fig. 15(c) illustrates that the frictional pressure drop obviously increases with the decrease of saturation pressure due to the increasing liquid-vapor density ratio resulting in enhancement of vapor-liquid shear force. Fig. 15(d) suggests that the influence of inclination angle on frictional pressure drop is slight.

It is important to accurately predict pressure drop of hydrocarbon mixture refrigerant in a spiral pipe for the design and optimization of SWHE. Therefore, four correlations of Friedel [48], Carter [49]; Fuchs [21] and Neeraas [20] were compared with simulated frictional pressure drop when Darcy-Weisbach Formula [50] coupling with Gnielinski method [51] was used to calculated the single-phase frictional pressure drop in a coiled tube. All frictional pressure drop correlations mentioned above were described in Table 8.

Fig. 16 shows the comparison between predicted results by the above correlations and simulation ones. The results show that Fuchs's correlation and modified Fuchs's correlation can well predict frictional pressure drop at all vapor qualities since two-phase enhancement factor was developed base on experimental data when vapor quality changed from 0 to 1. However, Friedel's correlation and Carter's correlation cannot well predict frictional pressure drop at low vapor qualities due to the fact that Friedel's correlation considered more shear force between vapor and liquid phase at low vapor qualities while Carter's correlation was proposed as pressure changed from 4.83 to 7.17 MPa, which is different from this study. ARD, MARD and percentage of data points correctly predicted of simulation cases within ±25% error for each correlation are given in Table 9. It indicates that modified Fuchs's correlation has the best agreement with simulation results, and the deviations are almost all within ±25% while ARD and MARD are −6.85% and 10.67%, respectively.

Therefore, modified Fuchs's correlation can be used to well predict condensation frictional pressure drop for ethane/propane mixture upward flow in a spiral pipe

4.4. Characteristics of condensation heat transfer

The characteristics of condensation heat transfer for ethane/propane mixture upward flow in a spiral pipe are discussed as

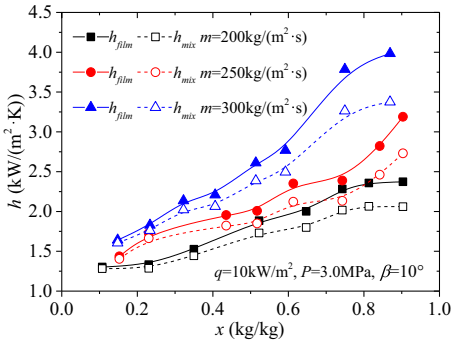

(a) Under different mass fluxes

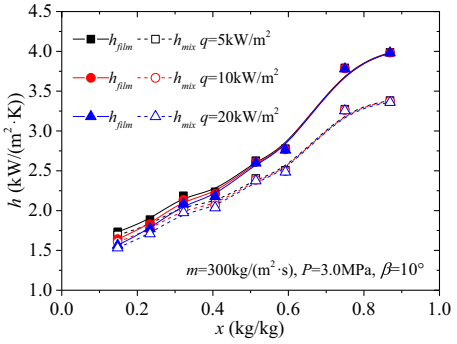

(b) Under different heat fluxes

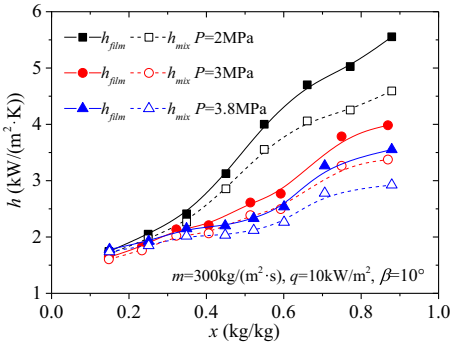

(c) Under different saturation pressure

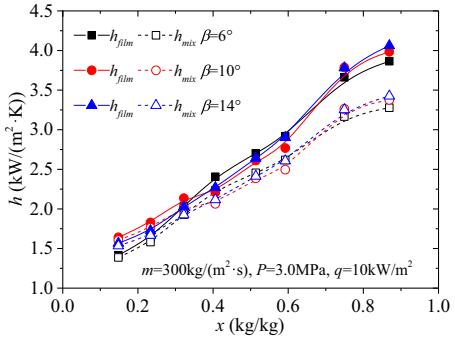

(d) Under different inclination angles

Fig. 17. Film and mixed heat transfer coefficients vs. vapor quality under different parameters.

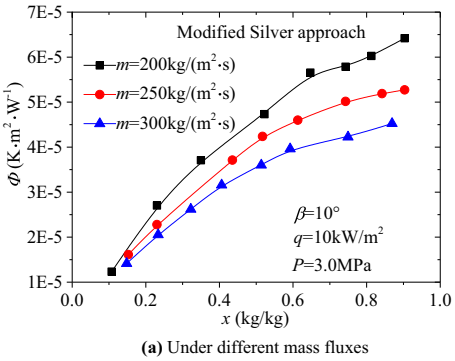

(a) Under different mass fluxes

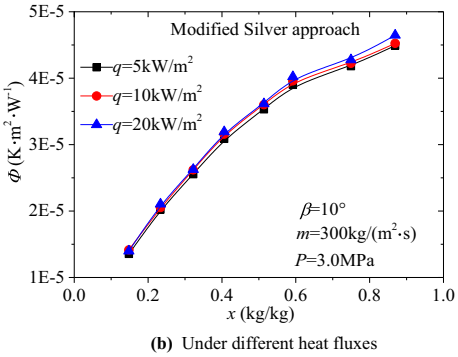

(b) Under different heat fluxes

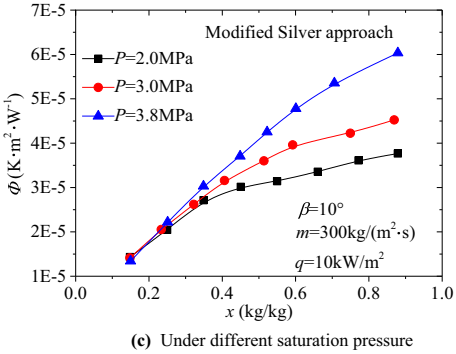

(c) Under different saturation pressure

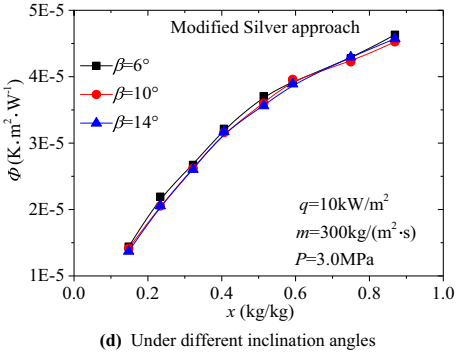

(d) Under different inclination angles

Fig. 18. Heat and mass transfer resistance in vapor core vs. vapor quality under different parameters.

follow when mass flux, heat flux, saturation pressure, inclination angle and vapor quality are from 200 to 300 kg/(m^2·s), 5 to 20 kW/m^2, 2.0 to 3.8 MPa, 6° to 14° and 0.1 to 0.9, respectively.

Fig. 17 displays the variation of film heat transfer coefficients and mixed heat transfer coefficients with vapor quality under different parameters. The results show that they both always increase as vapor quality increases but the increasing rates become slow under different parameters; this is because with the increasing vapor quality, the vapor-liquid velocity ratio increases so as to enhance the vapor-liquid shearing effect while the void fraction increases and then the liquid film become thinner, leading a smaller thermal resistance. By comparing h_{film} and h_{mix}, it is evident that mixed heat transfer coefficients are always smaller than film heat transfer coefficients especially at higher vapor qualities; it is due to

the existence of heat and mass transfer resistance in vapor core for hydrocarbon mixtures. Besides, Fig. 17(a) indicates that with the increase of mass flux, film heat transfer coefficients and mixed heat transfer coefficients both significantly increase especially at high vapor quality; just because vapor and liquid velocities both increase causing the enhancement of forced convective heat transfer. Meanwhile, Fig. 17(b) illustrates that film heat transfer coefficients and mixed heat transfer coefficients both slightly decrease with the increasing heat flux at low vapor qualities, but at high vapor quality, it has almost no influence on heat transfer; this dependence occurs because, when the vapor quality is small, full annular flow has not been formed, and then a larger heat transfer leading a larger driving temperature difference results in a thicker film at partial locations on the wall. Further, Fig. 17(c) explains that film heat transfer coefficients and mixed heat transfer coefficients both obviously increase with the decrease of saturation pressure due to the increasing liquid-vapor density ratio leading the enhancement vapor-liquid shearing effect and forced convective heat transfer in the liquid film. Fig. 17(d) shows that film heat transfer coefficients and mixed heat transfer coefficients both almost do not change with inclination angles.

The heat and mass transfer resistance in vapor core varies with vapor quality under different parameters is shown in Fig. 18.

From Fig. 18, it is clearly seen that heat and mass transfer resistance in vapor core continuously increases with vapor quality but the increasing rate becomes slow under different parameters, just because the ratio between sensible to total heat flux $Z \propto x$ while vapor-core heat transfer coefficient $h_{core} \propto x^{0.8}$, resulting in heat and mass transfer resistance in vapor core $\Phi \propto x^{0.2}$. Besides, Fig. 18(a) indicates that heat and mass transfer resistance in vapor core significantly decreases with the increasing mass flux especially at higher vapor qualities. This may be due to the fact that as the mass flux increases, the fluid is better mixed while the vapor-core heat transfer coefficient become larger, leading the vapor-core temperature closer to the interface temperature. Simultaneously, from Fig. 18(b) and (c), it is found that heat and mass transfer resistance in vapor core slightly increases with the increasing heat flux under the whole different vapor qualities while it obviously increases with the increase of saturation pressure at higher vapor qualities. Fig. 18(d) demonstrates that inclination angles affect heat and mass transfer resistance in vapor core little.

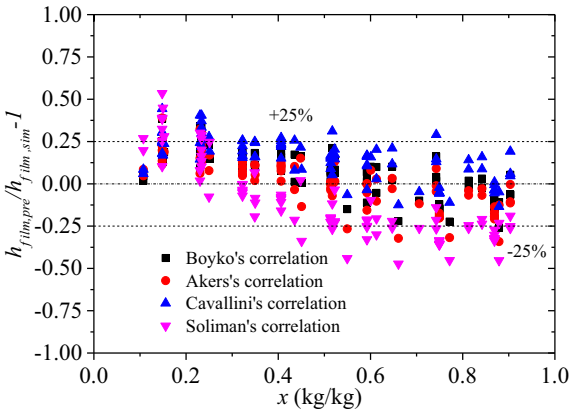

Fig. 19. Film heat transfer coefficients: comparison between the existing correlations and simulation results.

Table 11
ARD, MARD and percentage within ±25% error for above condensation heat transfer coefficient correlations.

Correlation	ARD	MARD	Percentage within ±25%
Boyko [22]	6.35%	13.06%	91.30%
Akers [52]	1.52%	12.24%	89.13%
Cavallini [53]	14.37%	16.61%	80.43%
Soliman [54]	−10.61%	22.47%	57.61%

Accurate heat transfer calculation of hydrocarbon refrigerant mixture in a spiral pipe is the basis to design and optimize SWHE. However, most of the existing condensation heat transfer correlations were developed based on single-component refrigerant; so their applicability to predict film condensation heat transfer coefficients for ethane/propane mixture upward flow in a spiral pipe needs further evaluation.

In this paper, four correlations of Akers [52], Boyko [22], Cavallini [53] and Soliman [54] were selected to compare with simulated film condensation heat transfer coefficients when Micheev correlation [55] and Aronow model [56] were used as single-phase heat transfer coefficient correlation in straight tubes and modified model in coiled tubes, respectively. All the heat transfer

Table 10
Description of correlation for heat transfer coefficient.

Authors	Heat transfer coefficient correlation
Micheev [55]	$h_{l0,s} = 0.021\frac{\lambda_l}{d}Re_{l0}^{0.8}Pr_l^{0.43}$
Aronow [56]	$\frac{h_{film,c}}{h_{film,s}} = 1 + 3.5\frac{d}{D}$
Akers [52]	$h_{film,s} = \begin{cases} 0.0265\frac{\lambda_l}{d}Re_{eq}^{0.8}Pr_l^{0.33}, & Re_{eq} > 5\times10^4 \\ 5.03\frac{\lambda_l}{d}Re_{eq}^{0.33}Pr_l^{0.33}, & Re_{eq} < 5\times10^4 \end{cases}$ $Re_{eq} = \frac{m[1-x+x(\rho_l/\rho_v)^{0.5}]d}{\mu_l}$
Boyko [22]	$h_{film,s} = \psi_{l0}h_{l0,s}, \psi_{l0} = \left(1-x+\frac{\rho_l}{\rho_v}x\right)^{0.5}$
Cavallini [53]	$h_{film,s} = \psi_{l0}h_{l0,s}$ $\psi_{l0} = 1 + 1.128x^{0.817}\left(\frac{\rho_l}{\rho_v}\right)^{0.3685} \times \left(\frac{\mu_l}{\mu_v}\right)^{0.2363}\left(1-\frac{\mu_v}{\mu_l}\right)^{2.144}Pr_l^{-0.1}$
Soliman [54]	$h_{film,s} = 0.036\frac{\lambda_l}{d}Re_{l0}Pr_l^{0.65}\left(\frac{\rho_l}{\rho_v}\right)^{0.5}\sqrt{\frac{0.023x^2}{Re_v^{0.2}}\phi_v^2 + Bo\sum_{n=1}^{5}a_n\left(\frac{\rho_v}{\rho_l}\right)^{\frac{n}{3}}}$ $\phi_v^2 = 1 + 2.85X_{tt}^2$ $X_{tt} = \left(\frac{1-x}{x}\right)^{0.9}\left(\frac{\rho_v}{\rho_l}\right)^{0.5}\left(\frac{\mu_l}{\mu_v}\right)^{0.1}, Re_v = \frac{mxd}{\mu_v}, Bo = \frac{q}{mi_{lv}}$ $a_1 = x(2-s)-1, a_2 = 2(1-x), a_3 = 2(s-1)(x-1)$ $a_4 = x^{-1}-3+2x, a_5 = s(2-x^{-1}-x), s = 1.25$ *for turbulent liquid film*

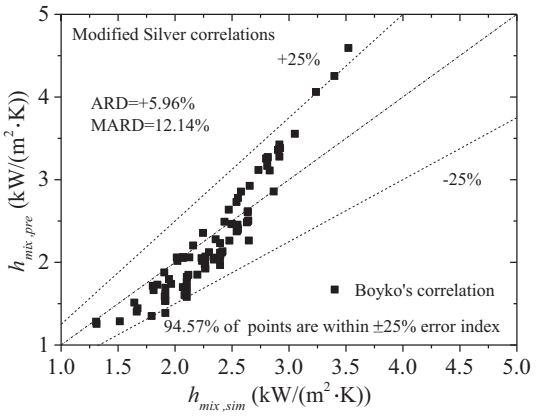

Fig. 20. Mixed heat transfer coefficient: comparison between Boyko's correlation together with modified Silver approach and simulation results together with modified Silver approach.

coefficients correlations mentioned above were described in Table 10.

Fig. 19 describes the comparison of film heat transfer coefficient between the results calculated by the above correlations and simulation ones. It is clearly seen that all correlations can well predict film heat transfer coefficients under the whole range of vapor quality except that Cavallini's and Soliman's correlations both over-predicts film heat transfer coefficients at low vapor qualities while Soliman's correlation slightly low-predicts film heat transfer coefficients at high vapor qualities. This is because Cavallini's and Soliman's correlations were both based on experimental data in annular flow while a lower velocity gradient in liquid film was taken in account at high vapor qualities in Soliman's correlation. ARD, MARD and percentage of data points correctly predicted of simulation cases within ±25% error for each correlation are given in Table 11. It indicates that Boyko's correlation can better conform to simulation results and their deviations are almost all within ±25%.

Fig. 20 displays the comparison on mixed heat transfer coefficient between predicted results by Boyko's correlation together with modified Silver approach and simulation results together with modified Silver approach. The result illustrates that almost all deviations are within ±25% while ARD and MARD are +5.96% and 12.14%, respectively. Therefore, Boyko's correlation together with modified Silver approach can be used to well predict mixed condensation heat transfer coefficients for ethane/propane mixture upward flow in a spiral pipe.

5. Conclusions

In this paper, a numerical model was established to investigate the condensation heat transfer and pressure drop characteristics for ethane/propane mixture upward flow in a spiral pipe. It discussed the typical flow patterns in the spiral pipe and the influence of vapor quality, mass flux, heat flux, saturation pressure and inclination angle on void fraction, frictional pressure drop, heat transfer coefficient and heat and mass transfer resistance. Comparing with the existing correlations, the better correlations for void fraction, film heat transfer coefficient and frictional pressure drop were selected. The important conclusions can be drawn as follows.

(1) The simulation results on frictional pressure drop and heat transfer coefficient both coincide with the experimental data from literatures and their deviations are within ±20% and ±15%, respectively. Meanwhile, the simulated flow patterns show good agreement with experimental ones.

(2) In this study, as the vapor quality increases, stratified flow, half-annular flow and annular flow are observed in order.

(3) The frictional pressure drop and film heat transfer coefficient both increase with the increase of vapor quality and mass flux but decrease with the increasing saturation pressure; and the heat flux and inclination angle both have little effect on them.

(4) For ethane/propane mixture, the mixed heat transfer coefficient h_{mix} shows the similar trend with film heat transfer coefficient h_{film}, but h_{mix} is always smaller than h_{film} especially at high vapor qualities; this is due to the existence of heat and mass transfer resistance in vapor core.

(5) The heat and mass transfer resistance in vapor core increases with the increase of vapor quality and heat flux but decreases as mass flux increases; with the increase of saturation pressure, the heat and mass transfer resistance in vapor core slightly decreases at low vapor qualities, but obviously increases at high vapor qualities; the influence of inclination angle is insignificant.

(6) Compared with other correlations, Steiner's correlation [44], modified Fuchs's correlation [20] and Boyko's correlation [22] together with modified Silver approach [20] show best agreement with simulation results on void fraction, frictional pressure drop and mixed heat transfer coefficient and their deviations are all almost within ±12%, ±25%, ±25%, respectively when m = 200–300 kg/(m^2 s), P = 2–3.8 MPa, x = 0.1–0.9, q = 5–20 kW/m^2 and β=6–14°.

Acknowledgment

The authors are grateful for the support of the research funds from 863 program on National High Technology Research and Development program (2013AA09A216) and the program of the Ministry of Industry and Information Technology in China ([2013]418).

Conflict of Interest

The authors declare that there is no conflict of interest regarding the publication of this article.

References

[1] J.C. Ho, N.E. Wijeysundera, S. Rajasekar, T.T. Chandratilleke, Performance of a compact, spiral coil heat exchanger, Heat Recovery Syst. CHP 15 (5) (1995) 457–468.
[2] J.C. Ho, N.E. Wijeysundera, Study of a compact spiral-coil cooling and dehumidifying heat exchanger, Appl. Therm. Eng. 16 (10) (1996) 777–790.
[3] N.E. Wijeysundera, J.C. Ho, S. Rajasekar, The effectiveness of a spiral coil heat exchanger, Int. Commun. Heat Mass Transfer 23 (5) (1996) 623–631.
[4] M.C. Weikl, K. Braun, J. Weiss, Coil-wound heat exchangers for molten salt applications, Energy Proc. 49 (2014) 1054–1060.
[5] H. Steffen, Near-Optimal Operation of LNG Liquefaction Processes by Means of Regulation, Berlin Institute of Technology, 2011, p. 17.
[6] M. Hammer, Dynamic Simulation of a Natural Gas Liquefaction Plant, Norwegian University of Science and Technology, Trondheim, 2004, p. 7.
[7] B.M. Fronk, S. Garimella, In-tube condensation of zeotropic fluid mixtures: a review, Int. J. Refrig. 36 (2) (2013) 534–561.
[8] N. Berrada, C. Marvillet, A. Bontemps, S. Daoudi, Heat transfer in-tube condensation of a zeotropic mixture of HFC23/HFC134a in a horizontal smooth tube, Int. J. Refrig. 7 (19) (1996) 463–472.
[9] D.W. Shao, E. Granryd, Experimental and theoretical study on flow condensation with non-azeotropic refrigerant mixtures of R32/R134a, Int. J. Refrig. 21 (3) (1998) 230–246.
[10] D.W. Shao, E.G. Granryd, Flow pattern, heat transfer and pressure drop in flow condensation part I: pure and azeotropic refrigerants, HVAC&R Res. 6 (2) (2000) 175–195.
[11] D.W. Shao, E.G. Granryd, Flow pattern, heat transfer and pressure drop in flow condensation Part II: zeotropic refrigerant mixtures (NARMs), HVAC&R Res. 6 (2) (2000) 197–209.
[12] S.J. Eckels, B.J. Unruh, Local heat transfer coefficients during condensation of R-22 and R-32/R-125 mixtures, HVAC&R Res. 5 (1) (1999) 59–76.

[13] F.J. Smit, J.P. Meyer, Condensation heat transfer coefficients of the zeotropic refrigerant mixture R-22/R-142b in smooth horizonal tubes, Int. J. Therm. Sci. 41 (7) (2002) 625–630.
[14] X. Huang, G. Ding, H. Hu, Y. Zhu, H. Peng, Y. Gao, B. Deng, Influence of oil on flow condensation heat transfer of R410A inside 4.18 mm and 1.6 mm inner diameter horizontal smooth tubes, Int. J. Refrig. 33 (1) (2010) 158–169.
[15] X. Huang, G. Ding, H. Hu, Y. Zhu, Y. Gao, B. Deng, Two-phase frictional pressure drop characteristics of R410A-oil mixture flow condensation inside 4.18 mm and 1.6 mm ID horizontal smooth tubes, HVAC&R Res. 16 (4) (2010) 453–470.
[16] X. Huang, G. Ding, H. Hu, Y. Zhu, Y. Gao, B. Deng, Condensation heat transfer characteristics of R410A–oil mixture in 5 mm and 4 mm outside diameter horizontal microfin tubes, Exp. Therm. Fluid Sci. 34 (7) (2010) 845–856.
[17] X. Huang, G. Ding, H. Hu, Y. Zhu, Y. Gao, B. Deng, Flow condensation pressure drop characteristics of R410A–oil mixture inside small diameter horizontal microfin tubes, Int. J. Refrig. 33 (7) (2010) 1356–1369.
[18] B. Thonon, A. Bontemps, Condensation of pure and mixture of hydrocarbons in a compact heat exchanger: experiments and modelling, Heat Transfer Eng. 23 (6) (2002) 3–17.
[19] M. Macdonald, S. Garimella, Hydrocarbon mixture condensation inside horizontal smooth tubes, Int. J. Heat Mass Transf. 100 (2016) 139–149.
[20] B.O. Neeraas, Condensation of Hydrocarbon Mixtures in Coil-wound LNG Heat Exchangers, Tube-side Heat Transfer and Pressure Drop, Ph.D. Thesis, Norwegian Institute of Technology, 1993.
[21] P.H. Fuchs, Pressure Drop and Heat Transfer during Flow of Evaporating Liquid in Horizontal Tubes and Bends, Ph.D. thesis, Norwegian Institute of Technology, 1975.
[22] L.D. Boyko, G.N. Kruzhilin, Heat transfer and hydraulic resistance during condensation of steam in a horizontal tube and in a bundle of tubes, Int. Heat Mass Transfer 10 (3) (1967) 361–373.
[23] L. Silver, Gas cooling with aqueous condensation, Trans. Inst. Chem. Eng 25 (1947) 30–42.
[24] J.K. Bell, M.A. Ghaly, An approximate generalized design method for multicomponent partial condensers, AIChE Symp Series, Heat Transfer 69 (131) (1973) 72–79.
[25] B.C. Price, J.K. Bell, Design of binary vapor condensers using the Colburn-Drew equations, AIChE Symp. Series 70 (138) (1974) 163–171.
[26] D. Sun, J. Xu, Q. Chen, Modeling of the evaporation and condensation phase-change problems with FLUENT, Numer. Heat Transfer, Part B: Fund. 66 (4) (2014) 326–342.
[27] Y. Kim, J. Choi, S. Kim, Y. Zhang, Effects of mass transfer time relaxation parameters on condensation in a thermosyphon, J. Mech. Sci. Technol. 29 (12) (2015) 5497–5505.
[28] S.K. Dahikar, A.A. Ganguli, M.S. Gandhi, J.B. Joshi, P.K. Vijayan, Heat transfer and flow pattern in co-current downward steam condensation in vertical pipes-I: CFD simulation and experimental measurements, Can. J. Chem. Eng. 91 (5) (2013) 959–973.
[29] H. Lee, C.R. Kharangate, N. Mascarenhas, I. Park, I. Mudawar, Experimental and computational investigation of vertical downflow condensation, Int. J. Heat Mass Transf. 85 (2015) 865–879.
[30] C.R. Kharangate, H. Lee, I. Park, I. Mudawar, Experimental and computational investigation of vertical upflow condensation in a circular tube, Int. J. Heat Mass Transf. 95 (2016) 249–263.
[31] F.R. Menter, Two-equation eddy-viscosity turbulence models for engineering applications, AIAA J. 32 (8) (1994) 1598–1605.
[32] G.D. Qiu, W.H. Cai, Z.Y. Wu, Y. Yao, Y.Q. Jiang, Numerical simulation of forced convective condensation of propane in a spiral tube, J. Heat Transfer 137 (4) (2015) 041502.
[33] M. Ishii, K. Mishima, Droplet entrainment correlation in annular two-phase flow, Int. J. Heat Mass Transf. 32 (10) (1989) 1835–1846.
[34] H.Y. Zhang, J.M. Li, J.L. Sun, B.X. Wang, Theoretical analysis for condensation heat transfer of binary refrigerant mixtures with annular flow in horizontal mini-tubes, Heat Mass Transf. 52 (1) (2016) 47–54.
[35] H. Deng, M. Fernandino, C.A. Dorao, Numerical study of heat and mass transfer of binary mixtures condensation in mini-channels, Int. Commun. Heat Mass Transf. 58 (2014) 45–53.
[36] H. Deng, M. Fernandino, C.A. Dorao, Numerical study of the condensation length of binary zeotropic mixtures, Energy Proc. 64 (2015) 43–52.
[37] R.M. Damle, P.M. Ardhapurkar, M.D. Atrey, Numerical investigation of transient behaviour of the recuperative heat exchanger in a MR J-T cryocooler using different heat transfer correlations, Cryogenics 80 (2016) 52–62.
[38] S.L. Li, W.H. Cai, J. Chen, H.C. Zhang, Y.Q. Jiang, Numerical study on the flow and heat transfer characteristics of forced convective condensation with propane in a spiral pipe, Int. J. Heat Mass Transf. 117 (2018) 1169–1187.
[39] J.U. Brackbill, D.B. Kothe, C. Zemach, A continuum method for modelling surface tension, J. Comput. Phys. 100 (1992) 335–354.
[40] E.W. Lemmon, M.L. Huber, M.O. Mclinden, NIST Standard Reference Database 23: Reference Fluid Thermodynamic and Transport Properties-REFPROP, Version 9.1, 2013.
[41] R.G. Sardesai, J.W. Palen, J. Taborek, Modified resistance proration method for condensation of vapor mixtures, AIChE Symp. Series 79 (225) (1983) 41–46.
[42] J. Yu, J. Chen, F. Li, W. Cai, L. Lu, Y. Jiang, Experimental investigation of forced convective condensation heat transfer of hydrocarbon refrigerant in a helical tube, Appl. Therm. Eng. 129 (2018) 1634–1644.
[43] M.A. Woldesemayat, A.J. Ghajar, Comparison of void fraction correlations for different flow patterns in horizontal and upward inclined pipes, Int. J. Multiph. Flow 33 (4) (2007) 347–370.
[44] D. Steiner, Heat Transfer to Boiling Saturated Liquids VDI-Warmeatla (VDI Heat Atlas), VDI-Gesellschaft Verfahrenstechnik und Chemieingenieurswesen (GCV), Düsseldorf, 1993.
[45] D. Chisholm, Void fraction during two-phase flow, J. Mech. Eng. Sci. 15 (3) (1973) 235–236.
[46] S.M. Zivi, Estimation of steady-state steam void-fraction by means of the principle of minimum entropy production, J. Heat Transfer 86 (2) (1964) 247–251.
[47] C.J. Baroczy, Correlation of Liquid Fraction in Two-Phase Flow with Application to Liquid Metals, Atomics International. Div. of North American Aviation Inc, Canoga Park, Calif, 1963.
[48] L. Friedel, Pressure drop during gas/vapor-liquid flow in pipes, Int. Chem. Eng. 20 (1980) 352–367.
[49] H.R. Carter, L.E. Johnson, G.B. Watson, Functional Performance of a Two-Tube Helically-Coiled Once-Through Steam Generator, ASME, 1976 (76-WA/HT-69).
[50] H. Yamaguchi, Engineering Fluid Mechanics, Springer Science & Business Media, 2008.
[51] V. Gnielinski, Correlations for the pressure drop in helically coiled tubes, Int. Chem. Eng. 26 (1) (1986) 36–44.
[52] W.W. Akers, H.A. Deans, O.K. Crosser, Condensing heat transfer within horizontal tubes, Chem. Eng. Prog. Symp. 55 (1959) 171–176.
[53] A. Cavallini, D.D. Col, L. Doretti, M. Matkovic, L. Rossetto, C. Zilio, G. Censi, Condensation in horizontal smooth tubes: a new heat transfer model for heat exchanger design, Heat Transfer Eng. 27 (8) (2006) 31–38.
[54] M. Soliman, J.R. Schuster, P.J. Berenson, A general heat transfer correlation for annular flow condensation, J. Heat Transfer 90 (2) (1968) 267–274.
[55] M.A. Micheev, Grundlagen der Wärmeübertragung, Verlag Technik, 1962.
[56] I.Z. Aronow, Heat Transfer in Liquid Flow in Coils, Teploenergetika 8 (6) (1961) 75–77.